Supporting Information for

Rapid solid-state metathesis reactions for the formation of cobalt-iron monoboride solid-solutions and investigation of their water splitting electrocatalytic activity

Janaka P. Abeysinghe, Edward G. Gillan*
Department of Chemistry, University of Iowa, Iowa City, Iowa 52242
E-mail: edward-gillan@uiowa.edu

Tables and Figures are ordered as they are first referenced in the main text of the paper.

List of Experimental, Tabular, and Graphical Supporting Information

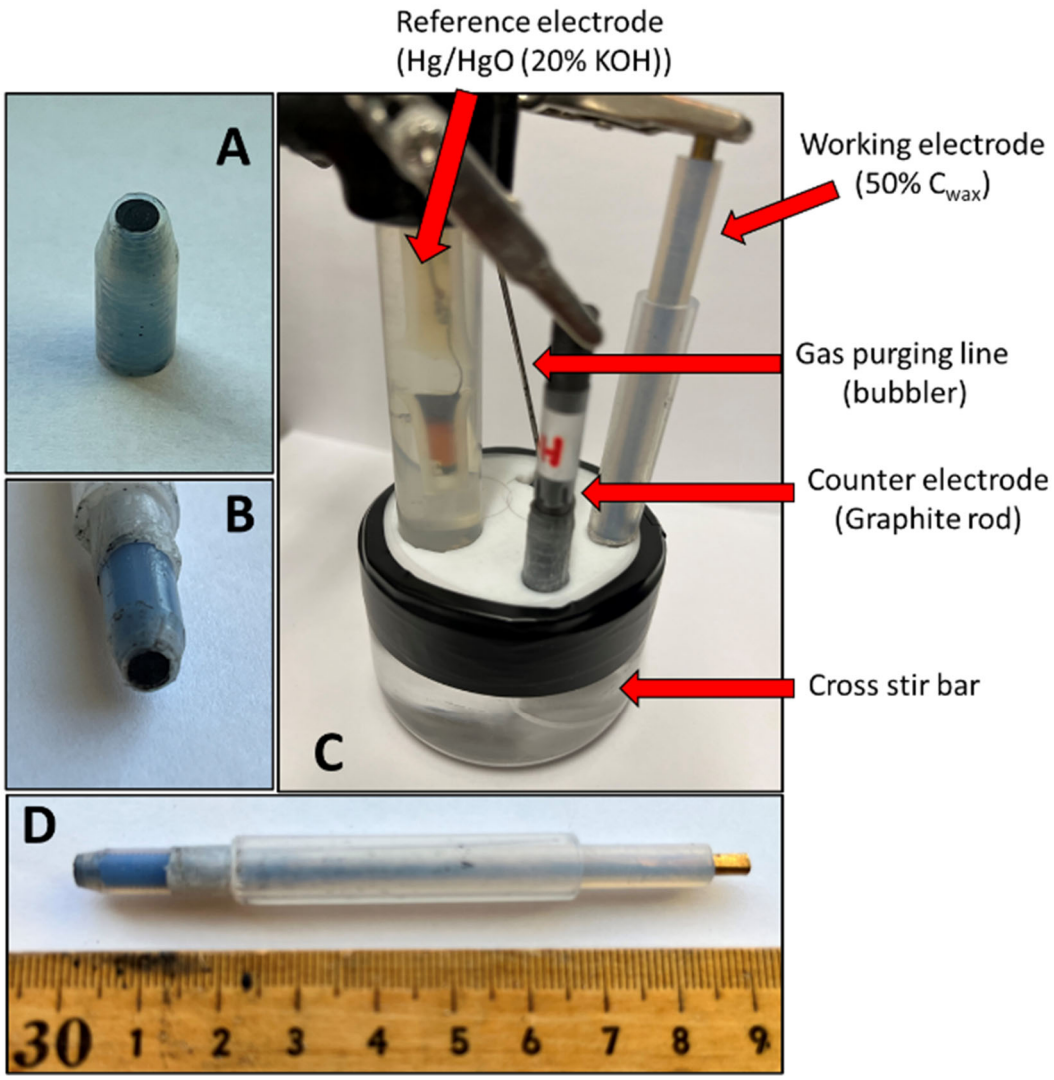

Figure S1. Images of electrochemical cell and electrode tip. (A) bare C_{wax} electrode tip (B) C_{wax} electrode tip with MB powder on it, (C) Three electrode electrochemical cell (working electrode-C_{wax}, counter electrode-graphite rod, reference electrode- Hg/HgO (20% KOH), bubbler, and cross stir bar, (D) assembled C_{wax} electrode tip+brass rod connector.

Table S1. Literature table for metal compounds synthesized from SSM reactions.
RT = room temperature; Filament initiation (ignition SSM) reactions can initiate at room temperature by passing a current through nichrome/ cu wire, however locally nichrome wire temperature rises to <=850 °C when passing the current and initiate the reaction. * Can be named as magnesiothermic reduction reaction as well. # Not a single-phase product.

Year	Material	Starting Materials	Initiation	Reaction Initiation Temp (°C)	Time	Ref.
1995	TiB_2, ZrB_2, HfB_2	MCl_x+MgB_2	Ampoule	850	18 h	1
	VB_2, NbB_2, TaB_2, FeB, CrB_2#, MoB_2#		Filament	RT	in sec	
2002	UB_4	UCl_4+MgB_2	Ampoule	850	1 day	2
2012	MB_6 (M=Ca, Ba, Sr)	MCl_2+MgB_2	quartz tube	850-900 (10^{-3} Torr)	12 hr	3
2013	CeB_6, NdB_6, SmB_6, EuB_6, GdB_6, YbB_6	$MCl_3.6H_2O+MgB_2$	Reactants in an Alsint boat covered by a silicon wafer and then inserted in a Quartz tube	650	1 hr	4
2017	MoB_2	$MoCl_5+MgB_2$	Quartz tube	650	24 hr	5
2019	CrB_2#, MnB_4, FeB, CoB	MCl_2+MgB_2		850	10 hr	6
	TiB_2, ZrB_2, HfB_2	MCl_4+MgB_2		850	10 hr	
	VB_2	VCl_3+MgB_2		850	10 hr	
	NbB_2, TaB_2, MoB_2	MCl_5+MgB_2		850	10 hr	
	WB_x	WCl_6+MgB_2		850	10 hr	
	ReB_2	$K_2ReCl_6+MgB_2$		850	10 hr	
	OsB_2#	$K_2OsCl_6+MgB_2$		1100	10 hr	
	RuB_2	$K_2RuCl_5+MgB_2$		950	3 hr	
2020	MB (M=V,Cr,Nb,Mo,Ru, Ta,W)	MCl_x+MgB_2+Mg*	Quartz tube	800-950	5-9 hr	7
2020	Ru_7B_3, RuB	$K_2RuCl_5+MgB_2+$ Mg*	Quartz tube	700-950	3-10 hr	8
	Ru_2B_3, RuB_2	K_2RuCl_5 +MgB_2				
2022	FeB, CoB, NiB#	MCl_x+MgB_2	Filament	RT	In sec	9
	FeB, CoB, NiB	$MCl_x+Mg+(x/2)B$ *				

Table S2. Unit cell parameters of CoB, FeB, and $Co_{1-x}Fe_xB$ crystalline systems.

	Co %	a (Å)	b (Å)	c (Å)	Cell volume (Å^3)
CoB standard pattern (PDF 04-003-2122)		3.948	5.243	3.037	62.9
CoB	100	3.9557	5.2498	3.0417	63.2
CoB (conv.)	100	5.2498	3.0417	3.9557	63.2
$Co_{0.8}Fe_{0.2}B$	80	5.3177	3.0166	3.9793	63.8
$Co_{0.6}Fe_{0.4}B$	60	5.3718	2.9949	3.9981	64.3
$Co_{0.5}Fe_{0.5}B$	50	5.3984	2.9806	4.012	64.6
$Co_{0.4}Fe_{0.6}B$	40	5.424	2.973	4.0276	64.9
$Co_{0.2}Fe_{0.8}B$	20	5.4713	2.9563	4.0454	65.4
FeB	0	5.5006	2.9476	4.0600	65.8
FeB standard pattern (PDF 04-013-1637)	0	5.504	2.945	4.056	65.7
$Co_{0.5}Fe_{0.5}B$ standard pattern (PDF 01-079-2846)	50	5.4042	2.9803	4.0072	64.5

CoB, FeB, and $Co_{0.5}Fe_{0.5}B$ ($CoFeB_2$) crystalize in the orthorhombic crystal system. However, space groups of CoB (Pnma) are different from FeB and $Co_{0.5}Fe_{0.5}B$ (Pnma). The unit cell growth of CoB along a, b, and c axis are different from FeB or $Co_{1-x}Fe_xB$ solid-solutions. The a, b, and c values of CoB swapped to match with FeB and $Co_{1-x}Fe_xB$ cell directions are also shown (blue-color values).

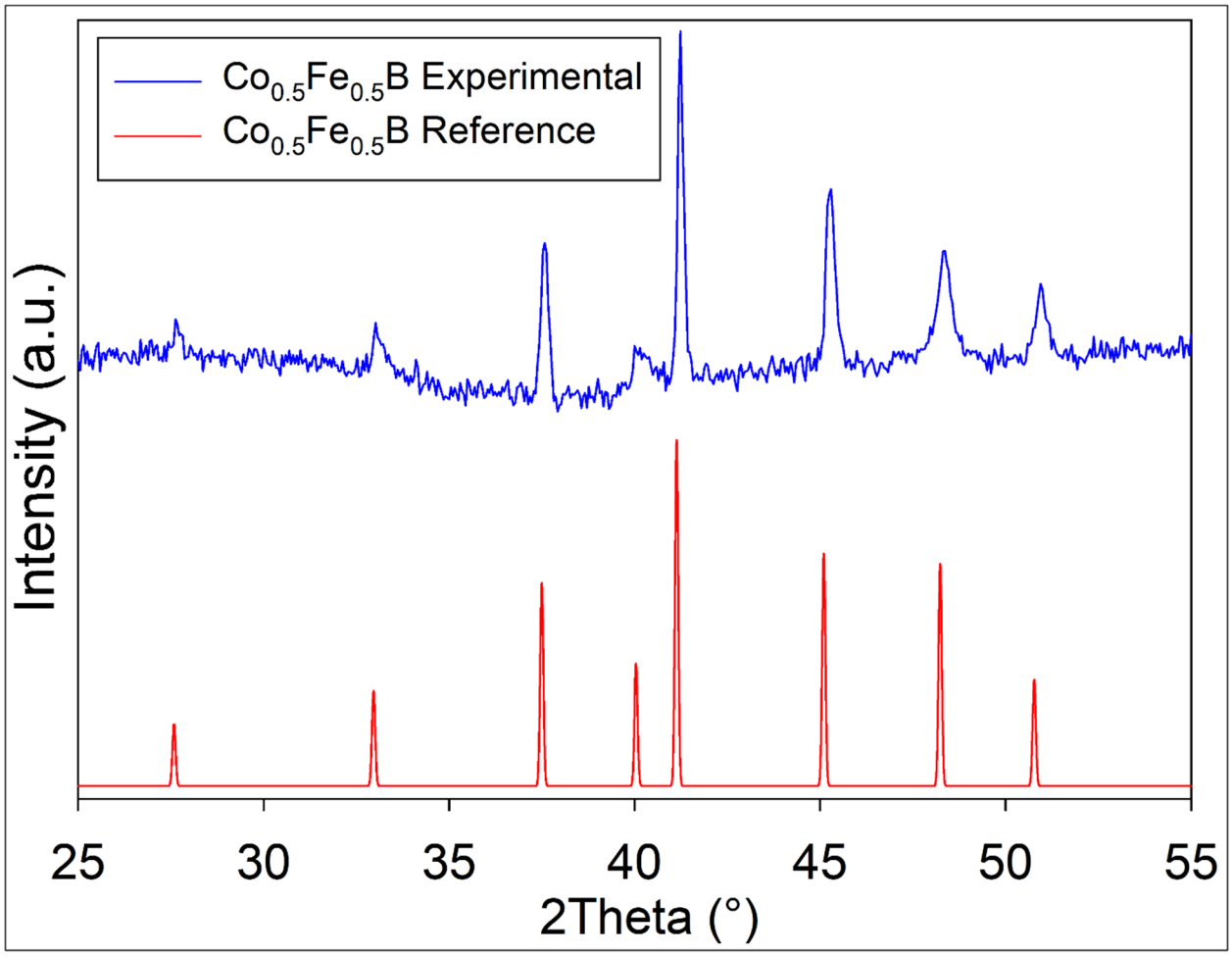

Figure S2. XRD comparison of experimentally obtained versus reference $Co_{0.5}Fe_{0.5}B$ (PDF 01-079-2846).

Table S3a. 2θ and d-spacing values of crystal planes (hkl) of FeB, $Co_{0.2}Fe_{0.8}B$, $Co_{0.4}Fe_{0.6}B$, and $Co_{0.5}Fe_{0.5}B$. Peak alignment was made using an internal Si standard.

	FeB		**$Co_{0.2}Fe_{0.8}B$**		**$Co_{0.4}Fe_{0.6}B$**		**$Co_{0.5}Fe_{0.5}B$**	
hkl	**d (Å)**	**2θ**	**d (Å)**	**2θ**	**d (Å)**	**2θ**	**d (Å)**	**2θ**
101	3.26656	27.3008	3.25282	27.4184	3.23360	27.5846	3.22012	27.6785
200	2.75030	32.5558	2.73565	32.7351	2.71200	33.0287	2.69919	33.1612
011	2.38526	37.7123	2.38688	37.6858	2.39193	37.6032	2.39258	37.5598
201	2.27703	39.5777	2.26614	39.7759	2.24955	40.0817	2.23953	40.2335
111	2.18837	41.2526	2.18775	41.2647	2.18857	41.2487	2.18737	41.2360
210	2.01089	45.0842	2.00788	45.1557	2.00360	45.2573	2.00071	45.2860
102	1.90445	47.7559	1.89720	47.9496	1.88788	48.2014	1.88039	48.3621
211	1.80198	50.6571	1.79853	50.7611	1.79389	50.9017	1.79044	50.9608
301	1.67103	54.9462	1.66262	55.2479	1.64943	55.7279	1.64188	55.9554
112	1.59962	57.6228	1.59669	57.7383	1.59371	57.8565	1.59035	57.9368
020	1.47380	63.0768	1.47815	62.8699	1.48650	62.4769	1.49028	62.2422

Table S3b. 2θ and d-spacing values of crystal planes (hkl) of $Co_{0.6}Fe_{0.4}B$, $Co_{0.8}Fe_{0.2}B$, and CoB.

	$Co_{0.6}Fe_{0.4}B$		**$Co_{0.8}Fe_{0.2}B$**		**CoB**		
hkl	**d (Å)**	**2θ**	**d (Å)**	**2θ**	**hkl**	**d (Å)**	**2θ**
101	3.20730	27.8154	3.18604	28.0047	**110**	3.15925	28.2471
200	2.68590	33.3590	2.65885	33.7084	**020**	2.62490	34.1577
011	2.39699	37.5209	2.40392	37.4086	**101**	2.41126	37.2905
201	2.22952	40.4575	2.21077	40.8159	**111**	2.19119	41.1972
111	2.18895	41.2411	2.19050	41.2107	**120**	2.18717	41.2764
210	1.99907	45.3655	1.98967	45.5919	**021**	1.98724	45.6509
102	1.87355	48.5939	1.86350	48.8728	**210**	1.85085	49.2290
211	1.78838	51.0698	1.78316	51.2300	**121**	1.77575	51.4594
301	1.63419	56.2934	1.61919	56.8622	**130**	1.60033	57.5946
112	1.58835	58.0703	1.58539	58.1893	**211**	1.58114	58.3607
020	1.49745	61.9693	1.50828	61.4758	**002**	1.52085	60.9135

Table S4. Co/Fe metal ratio comparison from ICP, XRF, and EDS results.

SSM reaction molar ratios	Final Products	Theoretical Co/Fe	ICP Co/Fe	XRF Co/Fe	EDS Co/Fe
4$CoCl_2$/$FeCl_2$/5Mg/10B	$Co_{0.8}Fe_{0.2}B$+B	80/20	81/19	78/22	78/22
3$CoCl_2$/2$FeCl_2$/5Mg/10B	$Co_{0.6}Fe_{0.4}B$+B	60/40	58/42	-	55/45
2.5$CoCl_2$/2.5$FeCl_2$/5Mg/10B	$Co_{0.5}Fe_{0.5}B$+B	50/50	48/52	49/51	45/55
2$CoCl_2$/3$FeCl_2$/5Mg/10B	$Co_{0.4}Fe_{0.6}B$+B	40/60	38/62	-	33/67
$CoCl_2$/4$FeCl_2$/5Mg/10B	$Co_{0.2}Fe_{0.8}B$+B	20/80	17/83	21/79	19/81

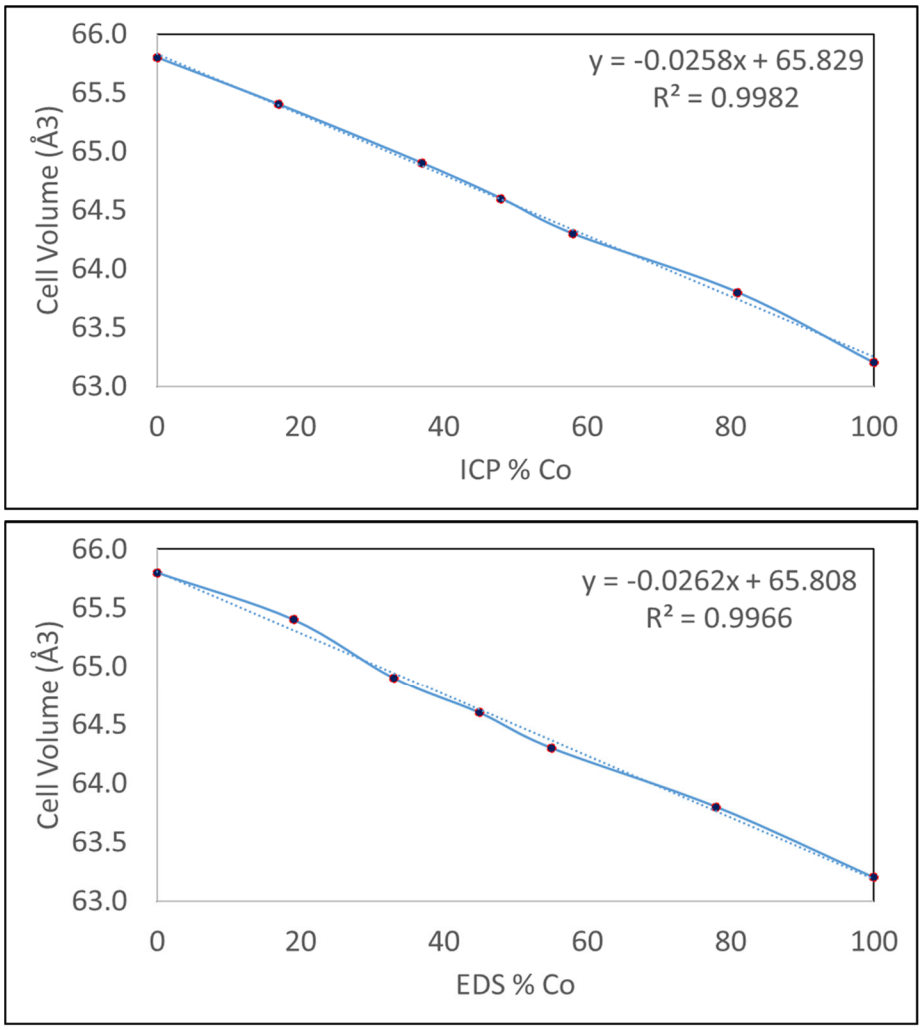

Figure S3. Unit cell volume changes with ICP and EDS measurements obtained %Co values of $Co_{1-x}Fe_xB$ solid-solutions. Dashed lines are linear regression results.

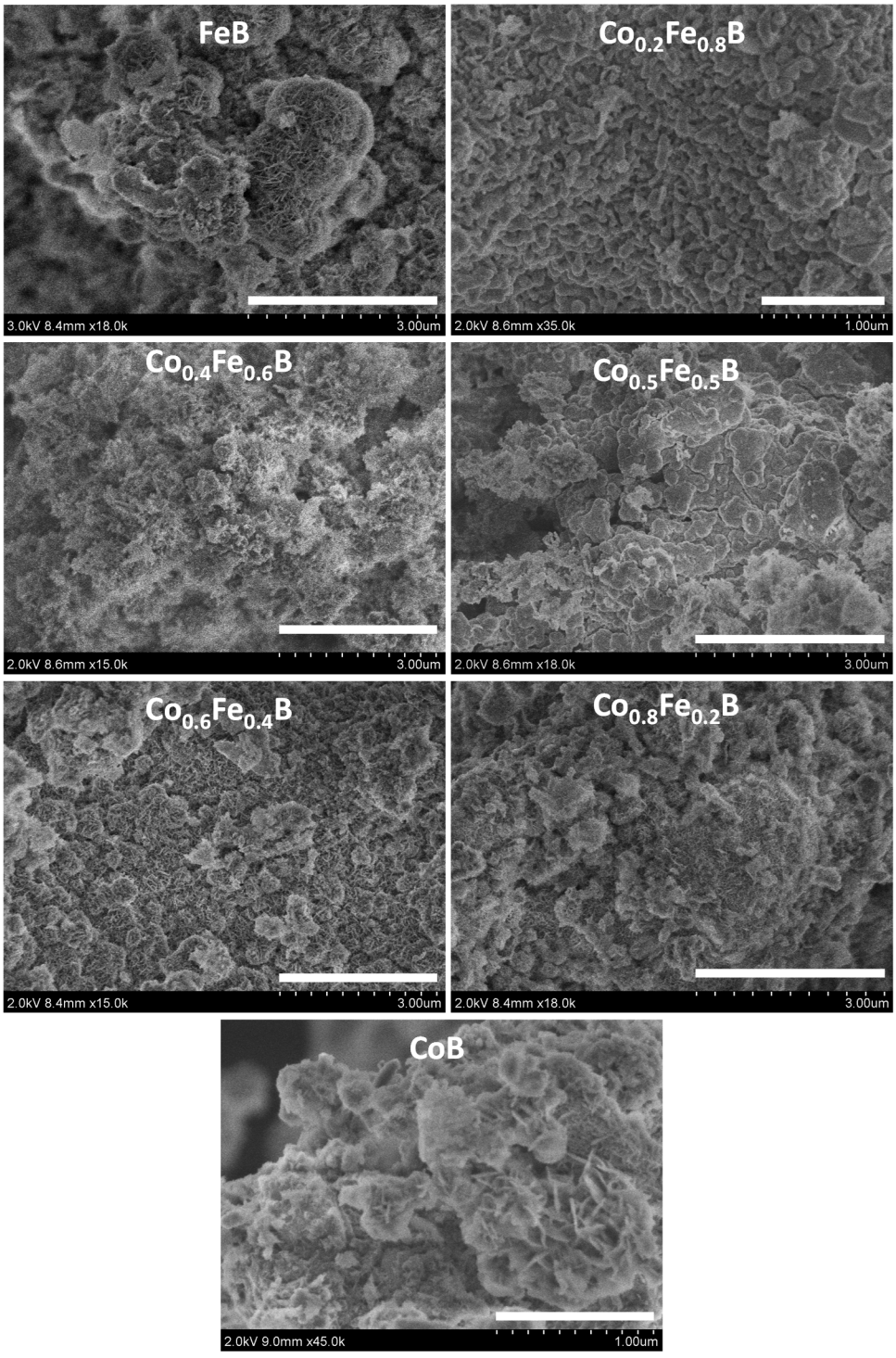

Figure S4. Additional high-magnification SEM images of FeB, $Co_{1-x}Fe_xB$ solid-solutions, and CoB. In all samples vertically grown plate-like structure morphology can be observed that may receive on metal boride surfaces after washing out $MgCl_2$ byproduct from product. The lengths of the scale bars: FeB, $Co_{0.4}Fe_{0.6}B$, $Co_{0.5}Fe_{0.5}B$, $Co_{0.6}Fe_{0.4}B$, and $Co_{0.8}Fe_{0.2}B$ are 3 μm and $Co_{0.2}Fe_{0.8}B$ and CoB are 1 μm.

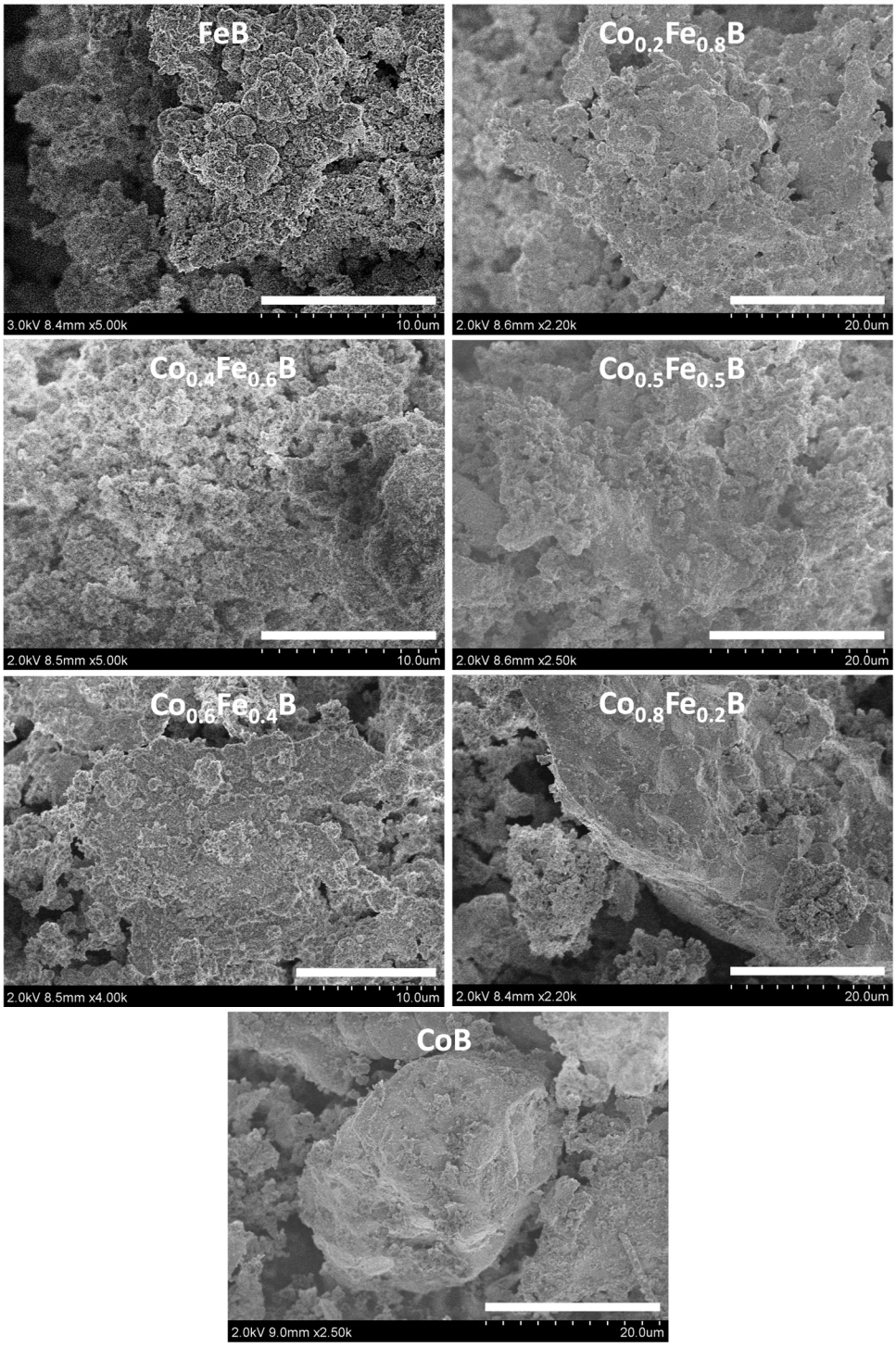

Figure S5. Low-magnification SEM images of FeB, $Co_{1-x}Fe_xB$ solid-solutions, and CoB. Apparent morphology transformation from aggregates of small and round-shaped FeB particles to large (μm-sized) monolithic blocks + aggregate particles of CoB through $Co_{1-x}Fe_xB$ solid-solutions can be seen from these low-magnification images. The lengths of the scale bars: FeB, $Co_{0.4}Fe_{0.6}B$, and $Co_{0.6}Fe_{0.4}B$ are 10 μm and $Co_{0.2}Fe_{0.8}B$, $Co_{0.5}Fe_{0.5}B$, $Co_{0.8}Fe_{0.2}B$, and CoB are 20 μm.

Table S5. The crystallite sizes of $Co_{1-x}Fe_xB$ solid-solutions determined by X-ray line broadening.

Metal boride	CoB	$Co_{0.8}Fe_{0.2}B$	$Co_{0.6}Fe_{0.4}B$	$Co_{0.5}Fe_{0.5}B$	$Co_{0.4}Fe_{0.6}B$	$Co_{0.2}Fe_{0.8}B$	FeB
Sample 1 (nm)	43.9	49.5	60.4	66.0	58.0	69.0	67.5
Sample 2 (nm)	52.5	50.9	60.4	73.4	61.4	60.8	62.0
Average (nm)	**48.2**	**50.2**	**60.4**	**69.7**	**59.7**	**64.9**	**64.8**

The (220) XRD peak at 47.3° 2θ of Si powder was used for instrument broadening and the (111) peaks of metal borides (41.236°) were used for the calculations. Two different sample scan results were obtained for each metal boride using Scherrer and Warren equations.

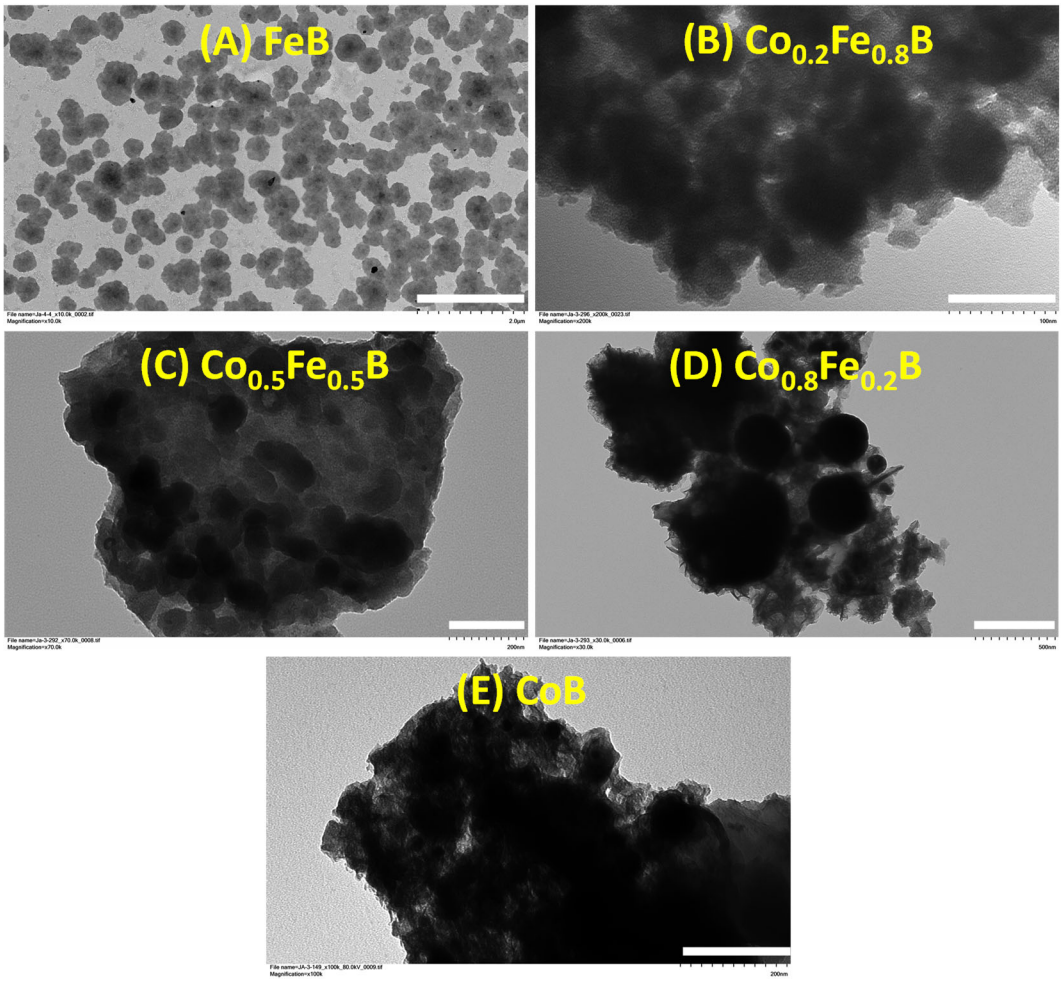

Figure S6. TEM images of FeB, CoB, and $Co_{1-x}Fe_xB$ solid-solutions. Scale bar length for images: (A) 2 μm, (B) 100 nm, (C) 200 nm, (D) 500 nm, (E) 200 nm.

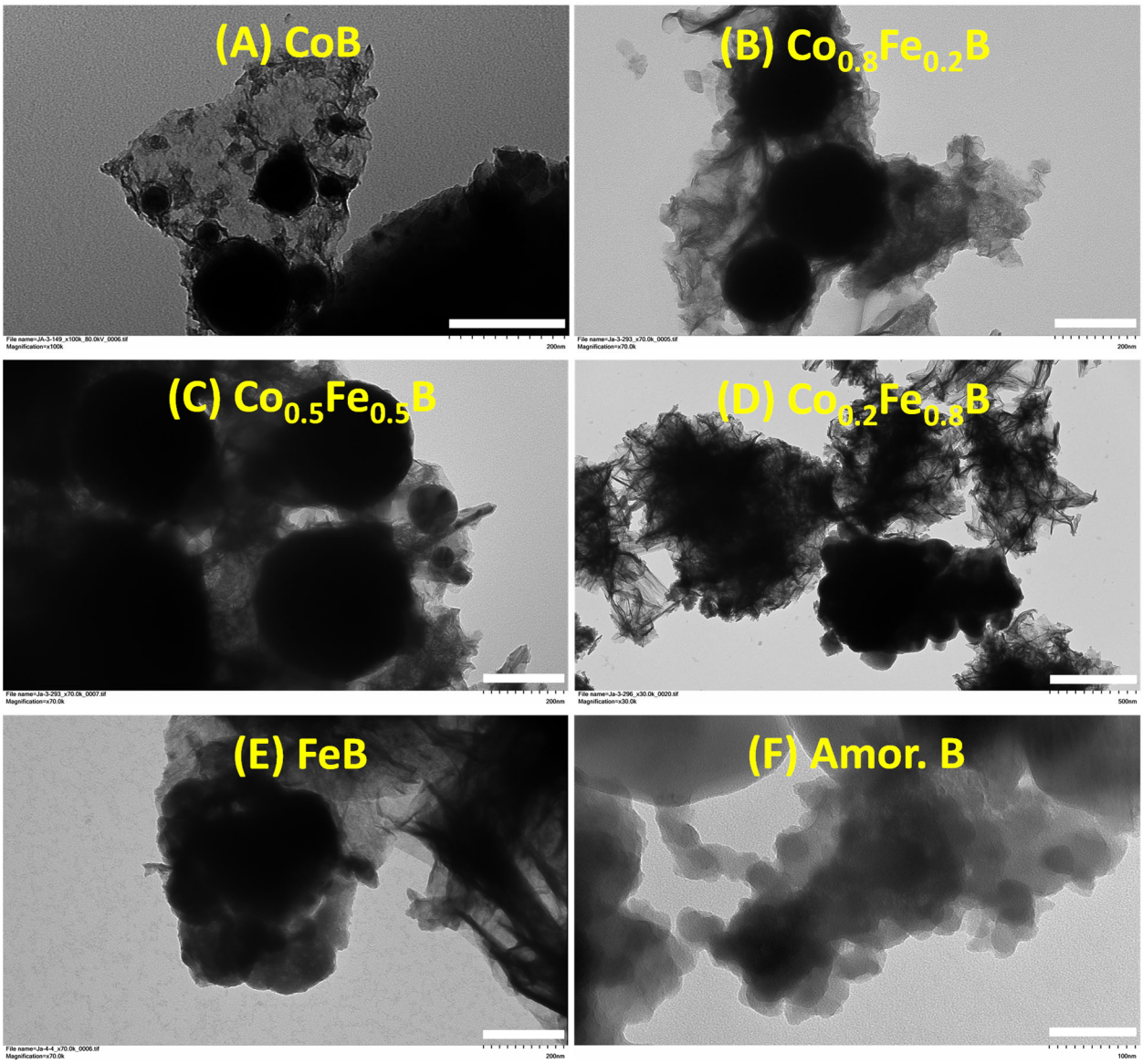

Figure S7. Additional TEM images of $Co_{1-x}Fe_xB$ solid-solutions, FeB, CoB, and amorphous B. Scale bar lengths: (A), (B), (C), (E) – 200 nm, (D) – 500 nm, (F) – 100 nm.

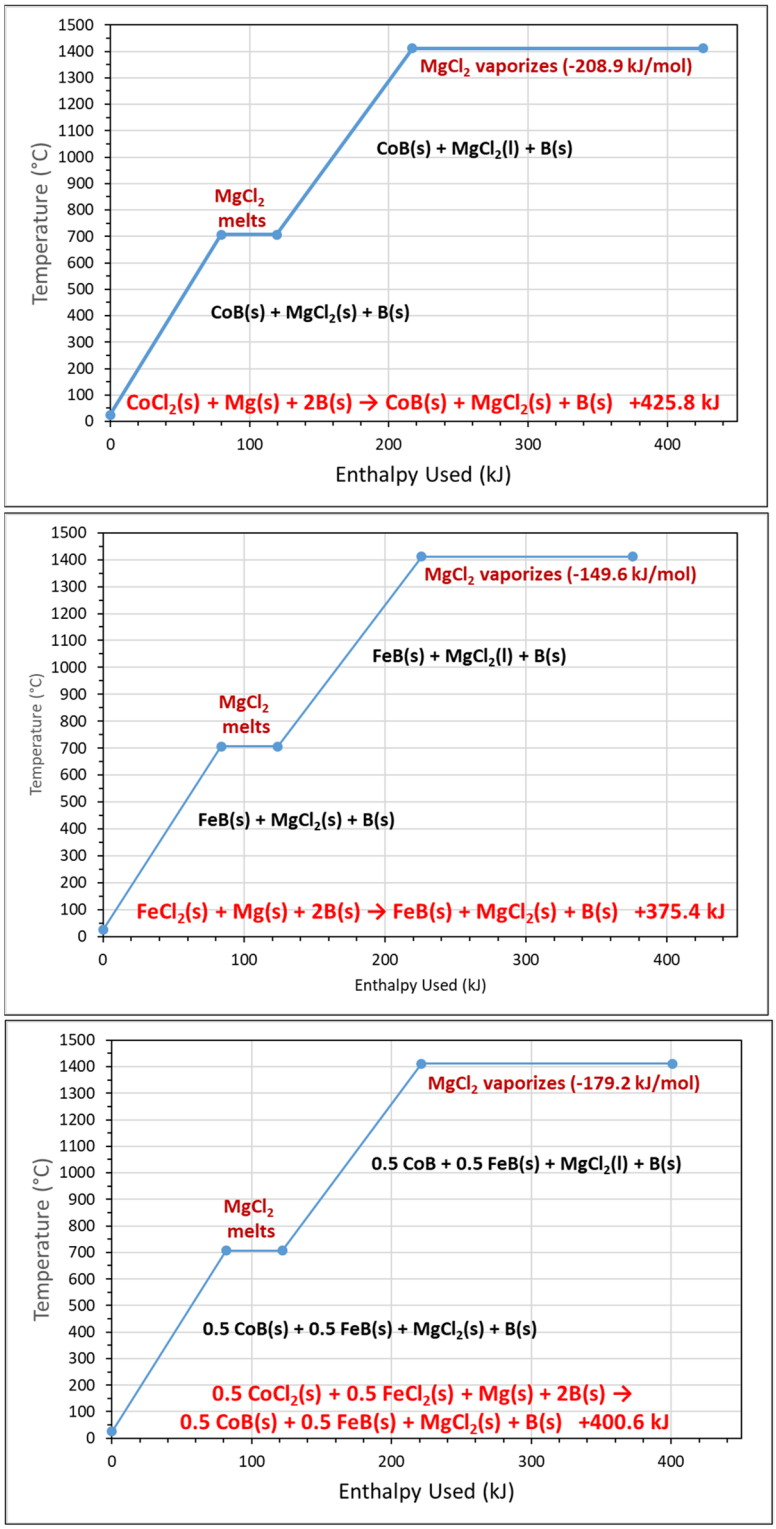

Figure S8. A plot of calculated adiabatic temperature data for CoB, FeB, and 0.5CoB+0.5FeB ($Co_{0.5}Fe_{0.5}B$) samples. Data points were calculated using the heat of reaction, standard heat capacities, and phase change energies. All three samples temperature-enthalpy graphs are very similar except reaction final step, $MgCl_2$ vaporization, acquired different enthalpies and resulting different % of $MgCl_2$ vaporizations (CoB: 100%, FeB: 72%, $Co_{0.5}Fe_{0.5}B$: 86%).

Sample calculations for reaction heat and adiabatic temperature

All thermochemical data of compounds were obtained from several thermochemical reference sources.[10, 11]

SSM reactions enthalpy calculations. An example of a thermochemical ΔH_{rxn} calculation that was done using Hess's Law for the $4CoCl_2/FeCl_2/5Mg/10B$ reaction. Since shortage of thermochemistry data of $Co_{1-x}Fe_xB$ solid solutions, CoB and FeB formation separately considered for the calculations.

	0.8 $CoCl_2$	+	0.2 $FeCl_2$	+	Mg	+	2B	→	0.8 CoB	+	0.2 FeB	+	$MgCl_2$	+	B
ΔH_f(kJ/mol)	-312.5		-341.6		0		0		-94.1		-72.8		-644.2		0

ΔH_{rxn} (kJ/mol CoB+FeB) $= \Sigma\Delta H_f$(products) - $\Sigma\Delta H_f$ (reactants) = -415.7

Maximum adiabatic reaction temperature (T_{ad}) calculations. For the T_{ad} calculations, complete reaction progress and no heat loss of reactions were assumed. Even though SSM reactions are very rapid, some heat loss from the reactor to the surrounding environment is possible in practice. As a result, actual maximum reaction temperatures may be lower than calculated adiabatic reaction temperatures (T_{ad}). The standard molar heat capacities (298 K and 1 atm) were used for solid compounds and molar heat capacities at melting and boiling temperatures were selected as the heat capacity of compounds in liquid and gas phases at 298 K.[10] Molar heat capacities of materials (mostly solids) generally increase with temperature, so the T_{ad} values represent upper limits of likely temperatures reached in these SSM reactions.

The T_{ad} calculation of $4CoCl_2/FeCl_2/5Mg/10B$ reaction.

	0.8 $CoCl_2$	+ 0.2 $FeCl_2$	+ Mg	+ 2 B	→	0.8 CoB	+ 0.2 FeB	+ $MgCl_2$	+ B	ΔH°_{rxn}	-415.7 (kJ/mol)
ΔH°_f (kJ/mol)	-312.5	-341.6	0	0		-94.1	-72.8	-644.2	0		
mp (C)	721	677	650	2077		1460	1590	707	2077		
bp (C)	1081	1020	1093	3866				1412	3866		
Heat of fusion (kJ/mol)						62.66	62.66	40.0			
Heat of vaporization (kJ/mol)								209.1			
C_p (j/mol K) (solid)						34.6	41.0	71.3	10.71		
C_p (j/mol K) (liquid)						61.5	68.3	92.8	31.75		
C_p (j/mol K) (gas)								57.1	20.8		

		ΔH =CpΔT
25 °C -707 °C	Products heat up to MgCl2 melting temp.	80.4
707 °C	$MgCl_2(s) \rightarrow MgCl_2(l)$	40.0
707 °C - 1412 °C	Products heat up to MgCl2 boiling temp.	98.3
1412 °C	$MgCl_2(l) \rightarrow MgCl_2(g)$	209.1

Final T_{ad} = 1412 °C

Table S6. Results for xCoCl$_2$ + (1-x)FeCl$_2$ + Mg rapid SSM reactions.

Reaction	% Yield based on target metal M	ΔH_f (kJ/mol)	Magnetic attraction
0.8CoCl$_2$ / 0.2FeCl$_2$/ Mg	55	-326	strong
0.5CoCl$_2$ / 0.5FeCl$_2$/ Mg	49	-317	strong
0.2CoCl$_2$ / 0.8FeCl$_2$/ Mg	46	-308	strong

All three products are ferromagnetic at room temperature, and they qualitatively show strong attraction to a permanent magnet.

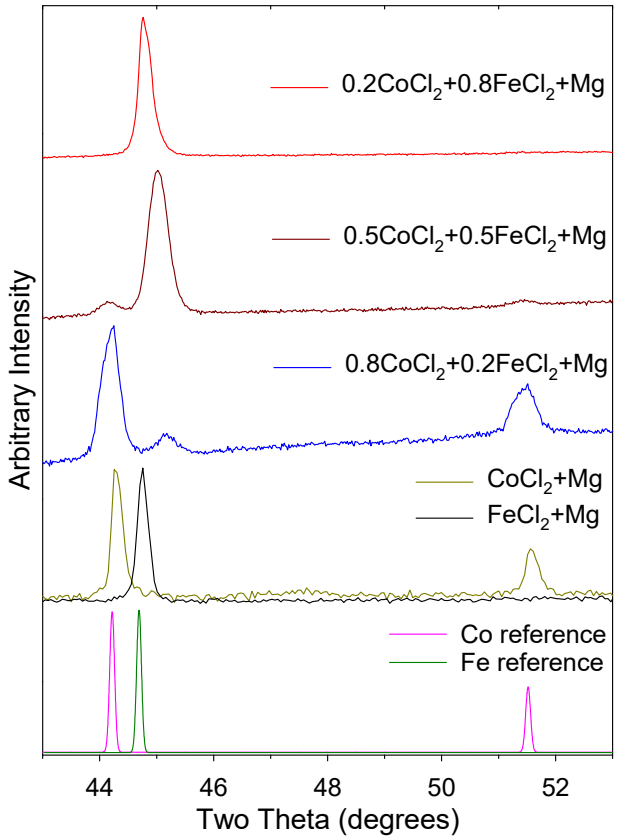

Figure S9. Powder XRD results of the (1-x)CoCl$_2$/xFeCl$_2$/Mg mechanistic study 1st half-reactions.

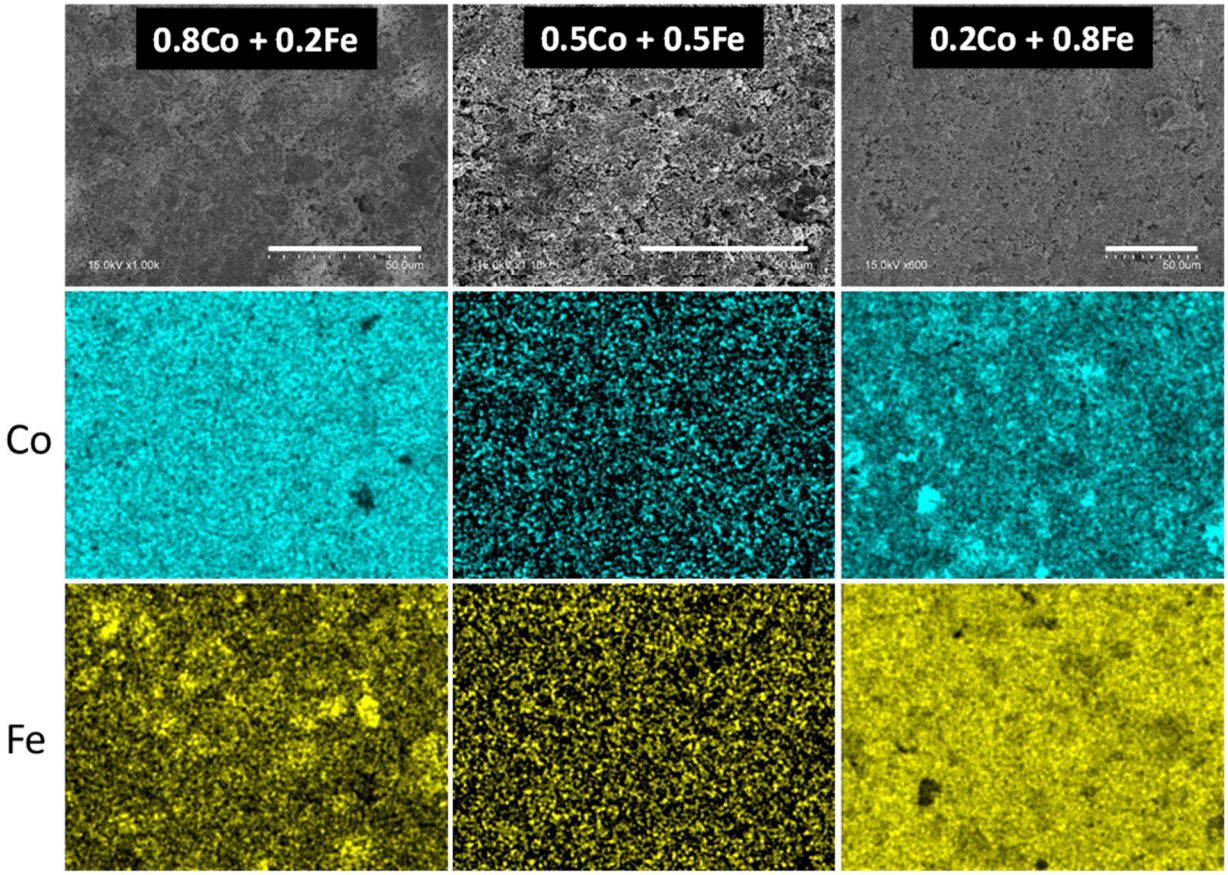

EDS analysis					
Co%	Fe%	Co%	Fe%	Co%	Fe%
90	10	59	41	30	70

Figure S10. EDS maps of (A) 0.8Co/0.2Fe, (B) 0.5Co/0.5Fe, and (C) 0.2Co/0.8Fe formed from x $CoCl_2$ + (1-x) $FeCl_2$+Mg mechanistic study reactions. The length of the scale bars are: (A, B, C) 50 μm.

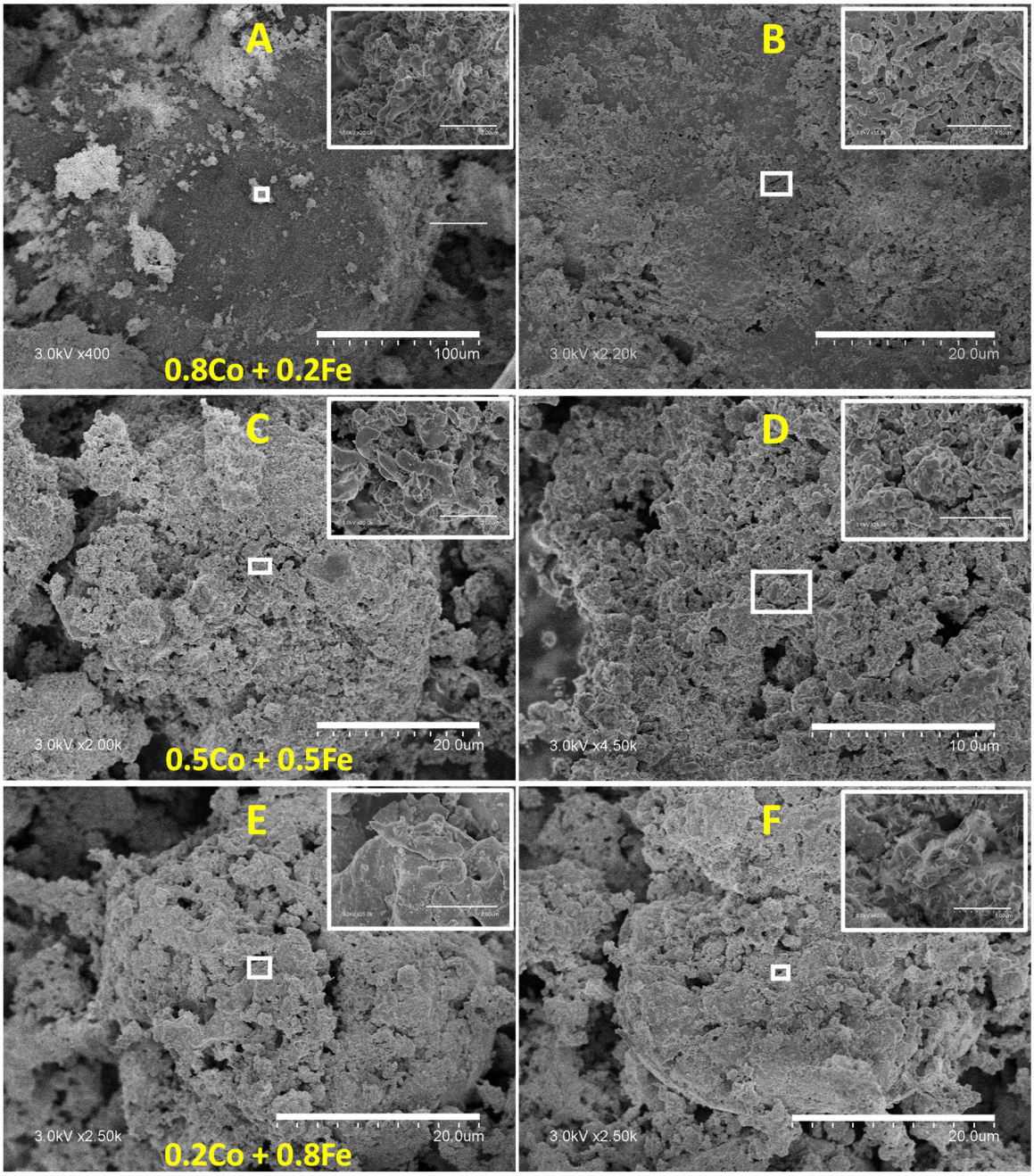

Figure S11. Scanning electron microscopy (SEM) comparison of particle morphologies obtained from SSM reactions of xCoCl$_2$ + (1-x)FeCl$_2$+Mg producing (A and B) 0.8Co/0.2Fe, (C and D) 0.5Co/0.5Fe, and (E and F) 0.2Co/0.8Fe (left column and right column are two representative SEM images of the same sample). Insets show a high magnification view of the highlighted white boxes in the low magnification images. The lengths of the scale bars are (main image, inset): (A) 100 µm and 2 µm, (B) 20 µm and 3 µm, (C) 20 µm and 2 µm, (D) 10 µm and 2 µm, (E) 20 µm and 2 µm, (F) 20 µm and 1 µm.

Table S7. Literature comparison table for crystalline and amorphous binary metal boride OER and HER activity in different electrolytes. All current densities are normalized for the geometric electrode area. The η_{10} overpotentials are calculated versus the ideal equilibrium 0 V and 1.23 V potentials for HER and OER water splitting.

MB (M= Fe, Co, Ni)	Electrode	OER (η_{10} mV)	HER (η_{10} mV)	Tafel slope (mV/dec) OER/HER	Electrolyte	Ref.
Crystalline metal borides (Co and Fe)						
CoB ($CoCl_2$/Mg/2B)	50% C_{wax}	345	-223	95/105	1.0 M KOH	this study
FeB ($FeCl_2$/Mg/2B)	50% C_{wax}	456	-395	52/136	1.0 M KOH	this study
FeB ($FeCl_3$/1.5MgB_2)	45% C_{wax}	418	-368	78/157	1.0 M KOH	[9]
FeB ($FeCl_3$/1.5Mg/B)	45% C_{wax}	480	-361	116/155	1.0 M KOH	[9]
CoB ($CoCl_2$/MgB_2)	45% C_{wax}	373	-293	54/109	1.0 M KOH	[9]
CoB ($CoCl_2$/Mg/2B)	45% C_{wax}	382	-279	69/100	1.0 M KOH	[9]
FeB_2	GC	296	-61	52/88	1.0 M KOH	[12]
Co_3B	CP	312		53	1.0 M KOH	[13]
Co_2B	GC	410		63	1.0 M KOH	[14]
Co_2B		380		45	0.1 M KOH	[15]
Co_2B	GC		-328	136, 177	1.0 M KOH	[15]
Co_2B	CP	287		51	1.0 M KOH	[13]
CoB	CP	340		63	1.0 M KOH	[13]
Crystalline metal borides (Other)						
NiB ($NiCl_2$/MgB_2)	45% C_{wax}	380	-312	72*/112	1.0 M KOH	[9]
NiB ($NiCl_2$/Mg/2B)	45% C_{wax}	346	-307	67*/111	1.0 M KOH	[9]
Ni_3B	-		-79	85	0.5 M H_2SO_4	[16]
NiB	GC	350		60	1.0 M KOH	[17]
Nano VB_2	CS		-192	68	0.5 M H_2SO_4	[18]
Bulk VB_2	CS		-348	126	0.5 M H_2SO_4	[18]
TiB_2	GC		-1070	196	0.5 M H_2SO_4	[19]
TiB_2	FTO	560			1.0 M $HClO_4$	[20]
TiB_2	GC		~-1100		0.5 M H_2SO_4	[21]
TiB_2-NaNAFT	GC		~-1000	146	0.5 M H_2SO_4	[21]
TiB_2-BuLi	GC		~-1000	158	0.5 M H_2SO_4	[21]
ZrB_2	GC		-970	173	0.5 M H_2SO_4	[19]
MoB/g-C_3N_4	GC		-152 (η_{20})	46	1.0 M KOH	[22]
MoB_2	CS		-154	49	0.5 M H_2SO_4	[5]
Mo_2B_5	GC		-740	118	0.5 M H_2SO_4	[23]
Mo_2B_5-BP treated	GC		-540	101	0.5 M H_2SO_4	[23]
RuB_2	GC		-28	29	1.0 M KOH	[6]
RuB_2	GC		-18	39	0.5 M H_2SO_4	[6]
RuB_2	GC		-35	28	0.5 M H_2SO_4	[24]
HfB_2	GC		-1050	194	0.5 M H_2SO_4	[19]
WB_2	GC		-203	65	0.5 M H_2SO_4	[24]
W_2B_5	GC		-680	115	0.5 M H_2SO_4	[23]
W_2B_5-BP treated	GC		-210	62	0.5 M H_2SO_4	[23]

Amorphous metal borides						
FeB	GC	392 (η_{20})		72	1.0 M KOH	[25]
Co_3B	GC	350 (η_{20})			1.0 M KOH	[26]
CoB pellet	-		-251	75	0.5 M KPi	[27]
CoB	GC		-203	79	0.5 M KPi	[28]
CoB	GC	344 (η_{20})		72	1.0 M KOH	[25]
CoB/C	GC	320		75	1.0 M KOH	[29]
CoB nanosheets	NF	265 (η_{20})		56	1.0 M KOH	[30]
CoB/NCNT		370		-	0.1 M KOH	[31]
CoB	Ni	140	-70	89/68	1.0 M KOH	[31]
Co-B@Co-Bi	GC	291		105	1.0 M KOH	[32]
CoB	GC	348		111	1.0 M KOH	[32]
Ni_3B-rGO films	CFP	290		88	1.0 M KOH	[33]
Ni_3B	CFP	340		81	1.0 M KOH	[33]
Ni_2B	GC	350		58	1.0 M KOH	[34]
NiB	GC		-132 (η_{20})	53, 112	1.0 M $HClO_4$	[35]
NiB	GC		-194 (η_{20})		1.0 M KOH	[35]
NiB	GC		-309	186	0.5 M KPi	[28]
Ni_2B/g-C_3N_4	GC		-707	221	1.0 M KOH	[36]
Ni-B@Ni-Bi	GC	310		150	1.0 M KOH	[32]
NiB	GC	365		100	1.0 M KOH	[32]
NiB	GC	331 (η_{20})		52	1.0 M KOH	[25]

50% C_{wax} = 50% graphite/50% paraffine wax, 45% C_{wax} = 45% graphite/55% paraffin wax, GC = glassy carbon, CP = carbon paper, CS = carbon sheet, FTO = fluorinated tin oxide glass, CFP = carbon fiber paper, NF = nickel foam *Approximate values due to pre-oxidation peaks having overlap with OER onset.

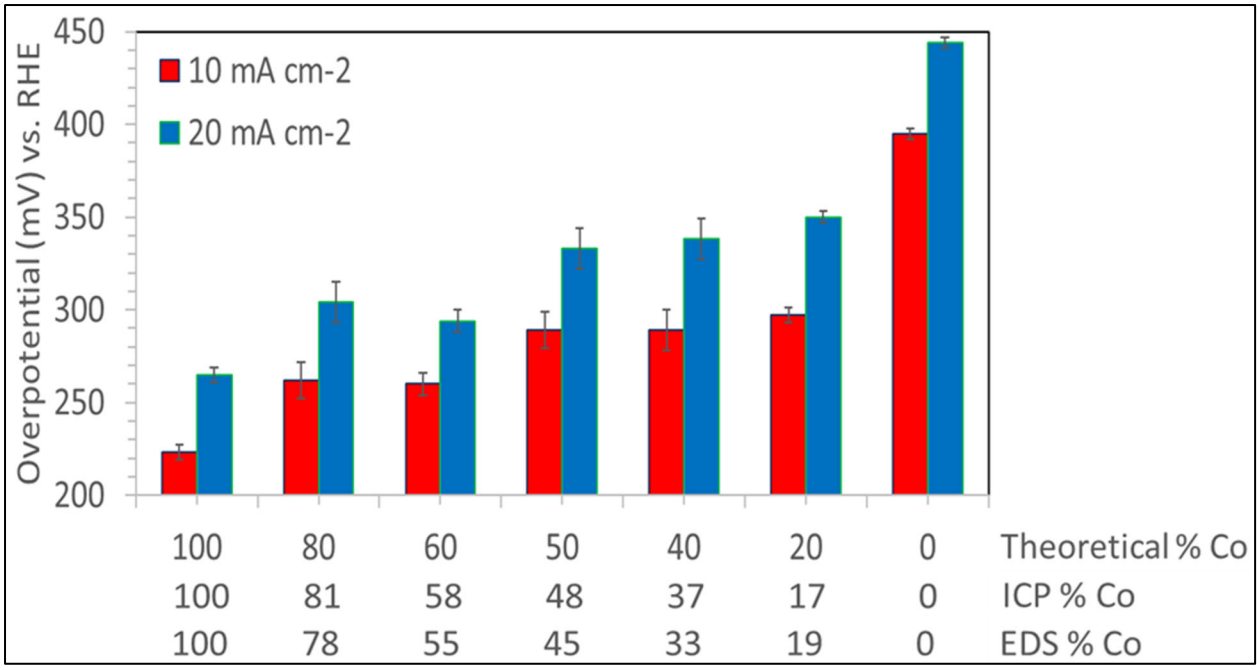

Figure S12. Graph of HER overpotentials at 10 mA cm^{-2} and 20 mA cm^{-2} current densities versus % Co (theoretical, ICP, and EDS).

Table S8. Literature comparison table for crystalline and amorphous ternary metal boride OER and HER activity in different electrolytes. All current densities are normalized for the geometric electrode area. The η_{10} overpotentials are calculated versus the ideal equilibrium 0 V and 1.23 V potentials for HER and OER water splitting.

MB	Crystalline/ amorphous	Electrode	OER (η_{10} mV)	HER (η_{10} mV)	Tafel slope (mV/dec) OER/HER	Electrolyte	Ref.
CoB $Co_{0.8}Fe_{0.2}B$ $Co_{0.6}Fe_{0.4}B$ $Co_{0.5}Fe_{0.5}B$ $Co_{0.4}Fe_{0.6}B$ $Co_{0.2}Fe_{0.8}B$ FeB	Cry	50% C_{wax}	345 351 340 338 353 403 456	223 262 288 289 289 297 392	95/105 66/139 79/163 103/150 87/160 78/177 52/169	1.0 M KOH	This study
Co_2MoB_4 Fe_2MoB_4	Cry	C_{cloth}	283 463	-	19.9 95.5	1.0 M KOH	[37]
Activated $FeCoB_2$	Cry	GCE	295	-	~84	1.0 M KOH	[38]
CoFeB CoB FeB	amor	NF	270 (η_{50}) 296 (η_{50}) 343 (η_{50})	-	36 109 68	1.0 M KOH	[39]
CoFeB CoB	Cry	GE	328 313	-	78.9 75.7	1.0 M KOH	[40]
NiFe-boride	amor	NF	167	-	25	1.0 M KOH	[41]
Co-Fe-B Co3-Fe-B Co-Fe3-B CoB FeB	Cry	-	280 330 360 400 450	129 194 201 212 267	38.9/67.3 65.4/94.6 66.7/79.5 65.9/86.8 58.4/99.9	1.0 M KOH	[42]
Fe_3Co_7B/CNT Fe_3Co_7B CoB/CNT FeB/CNT	Amor	GC	265 282 338 347	-	30 34 73 52	1.0 M KOH	[43]
$AlFe_2B_2$	Cry	NF	240	-	42	1.0 M KOH	[44]
NiCoFeB NiCoB CoB	Amor	GC	284 375 383	345 363 396	47/98 78.1/102 79/119	1.0 M KOH	[45]
CoNiB/CC	Amor	CC	-	80	88.2	1.0 M KOH	[46]
Co-3MoB	Amor	GC	96 66	- 320	56 155/67	KPi (pH 7) 1.0 M NaOH (pH 14)	[47]
Co2-Fe-B Co_2B Fe_2B	Amor	Cu sheet	298 340 472	-	62.6 97.3 81.6	1.0 M KOH	[48]

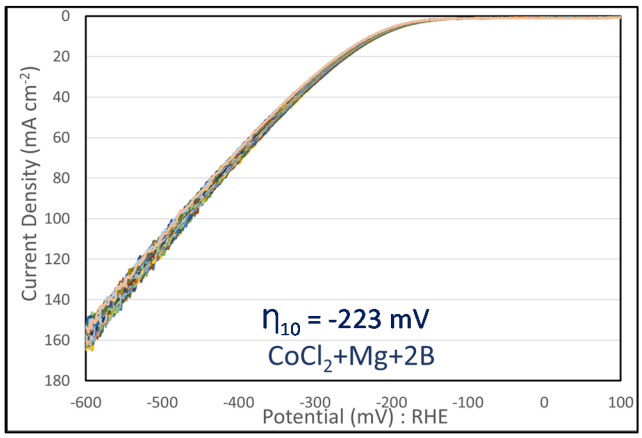
Current Density (mA cm-2)
Potential (mV) : RHE
η10 = -223 mV
CoCl2+Mg+2B

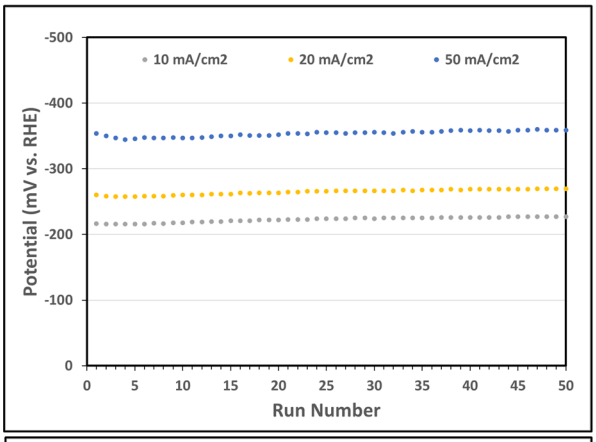
10 mA/cm2
20 mA/cm2
50 mA/cm2
Potential (mV vs. RHE)
Run Number

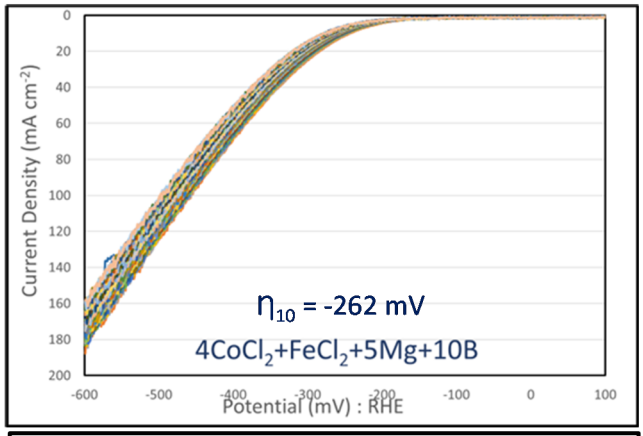
Current Density (mA cm-2)
Potential (mV) : RHE
η10 = -262 mV
4CoCl2+FeCl2+5Mg+10B

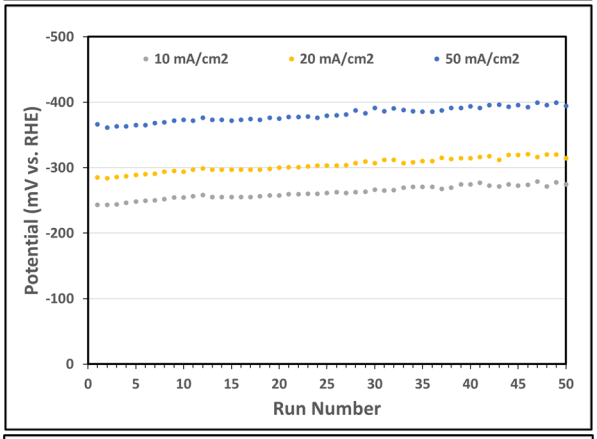
10 mA/cm2
20 mA/cm2
50 mA/cm2
Potential (mV vs. RHE)
Run Number

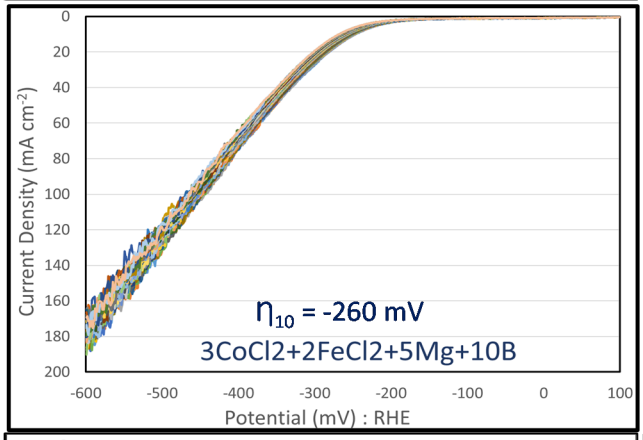
Current Density (mA cm-2)
Potential (mV) : RHE
η10 = -260 mV
3CoCl2+2FeCl2+5Mg+10B

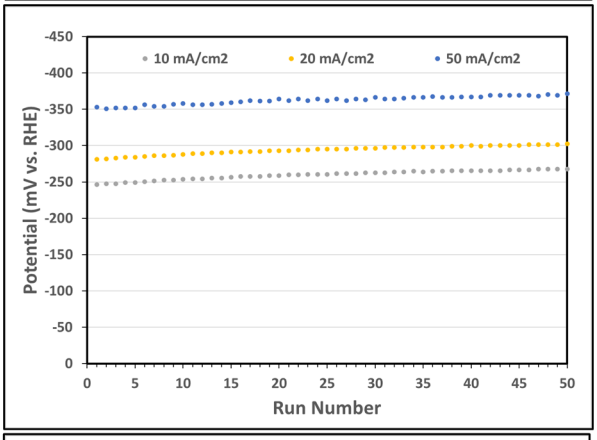
10 mA/cm2
20 mA/cm2
50 mA/cm2
Potential (mV vs. RHE)
Run Number

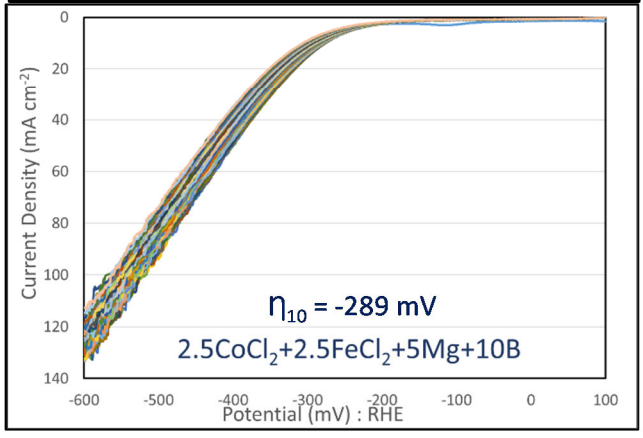
Current Density (mA cm-2)
Potential (mV) : RHE
η10 = -289 mV
2.5CoCl2+2.5FeCl2+5Mg+10B

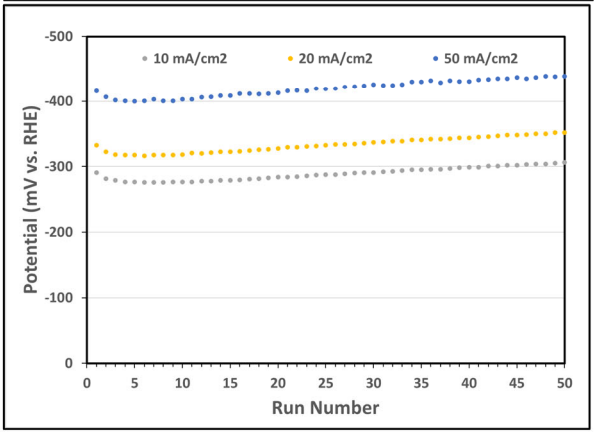
10 mA/cm2
20 mA/cm2
50 mA/cm2
Potential (mV vs. RHE)
Run Number

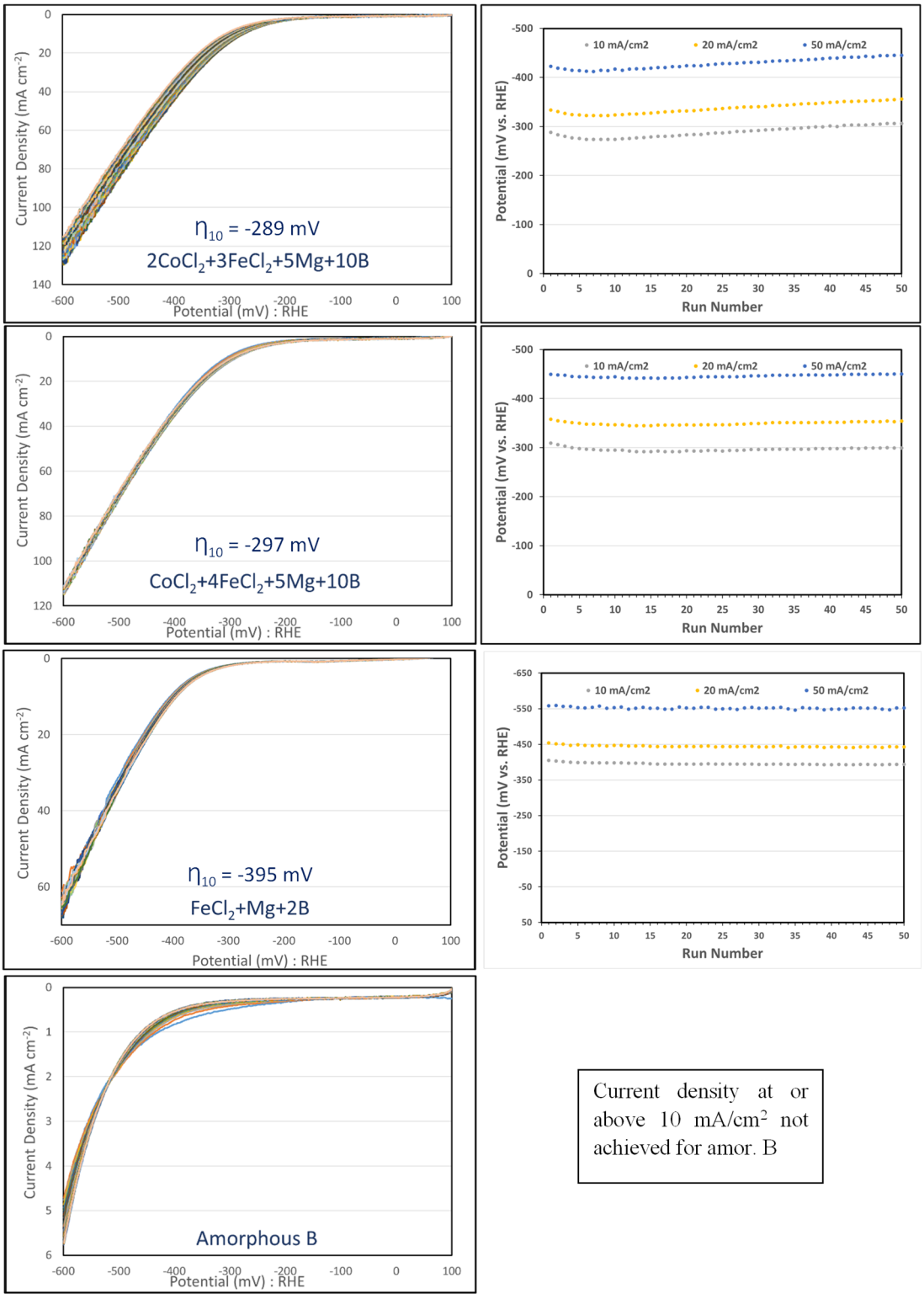

Figure S13. Left column: Overlay plots of 50 LSV scans of metal borides for HER in 1.0 M KOH at 5 mV s^{-1} scan rate. Right column: Plots of run number versus potentials at 10, 20, and 50 mA/cm^2 current densities extracted from left column overlay plots. Metal boride powders are embedded on C_{wax} working electrodes.

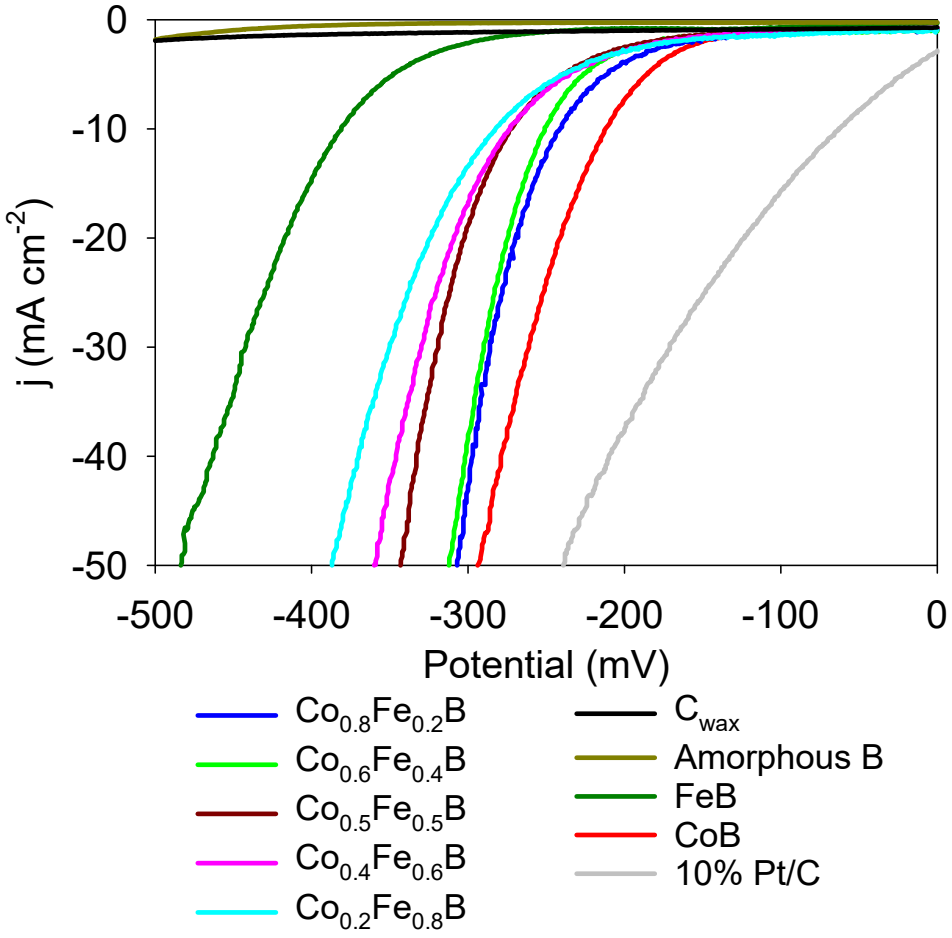

Figure S14. HER LSV overlay plots for metal borides with 85% iR compensation at 5 mV s^{-1} scan rate. A representative LSV run from 10 LSVs with iR on is shown in the graph. The working electrodes are metal boride powders embedded on C_{wax} tips.

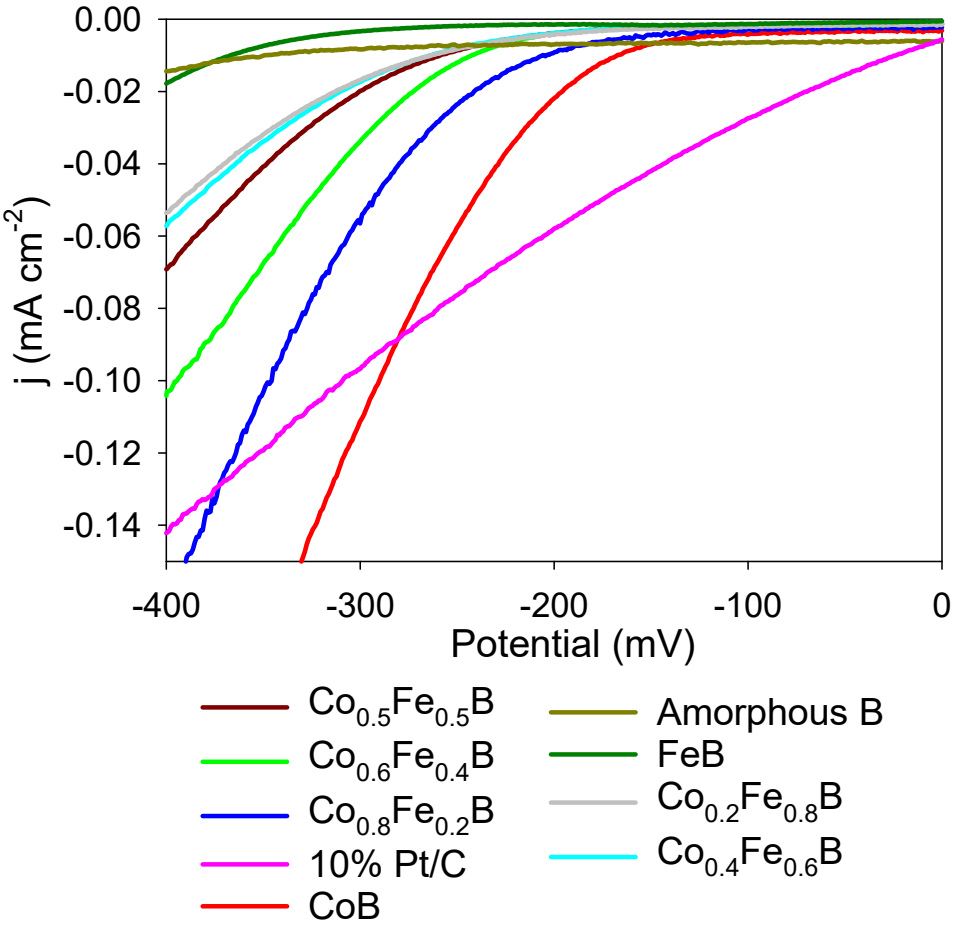

Figure S15. HER LSV overlay plots for metal borides and 10% Pt/C with ECSA normalized current densities in 1.0 M KOH.

Table S9. HER electrocatalysis of CoB + FeB physical mixing samples in 1.0 M KOH (average of 50 HERs were reported in the table).

Sample	(η_{10}) (mV)[1]	(η_{20}) (mV)	Tafel (mV dec^{-1})	ECSA (cm^2)
CoB	-223 ± 4	-265 ± 4	-105	22
4 CoB + FeB	-293 ± 1	-355 ± 1	-121	23
3 CoB + 2 FeB	-298 ± 1	-356 ± 2	-139	29
2.5 CoB + 2.5 FeB	-305 ± 1	-372 ± 2	-148	54
2 CoB + 3 FeB	-313 ± 2	-378 ± 2	-153	35
CoB + 4 FeB	-364 ± 5	-430 ± 6	-155	31
FeB	-395 ± 3	-444 ± 3	-136	43

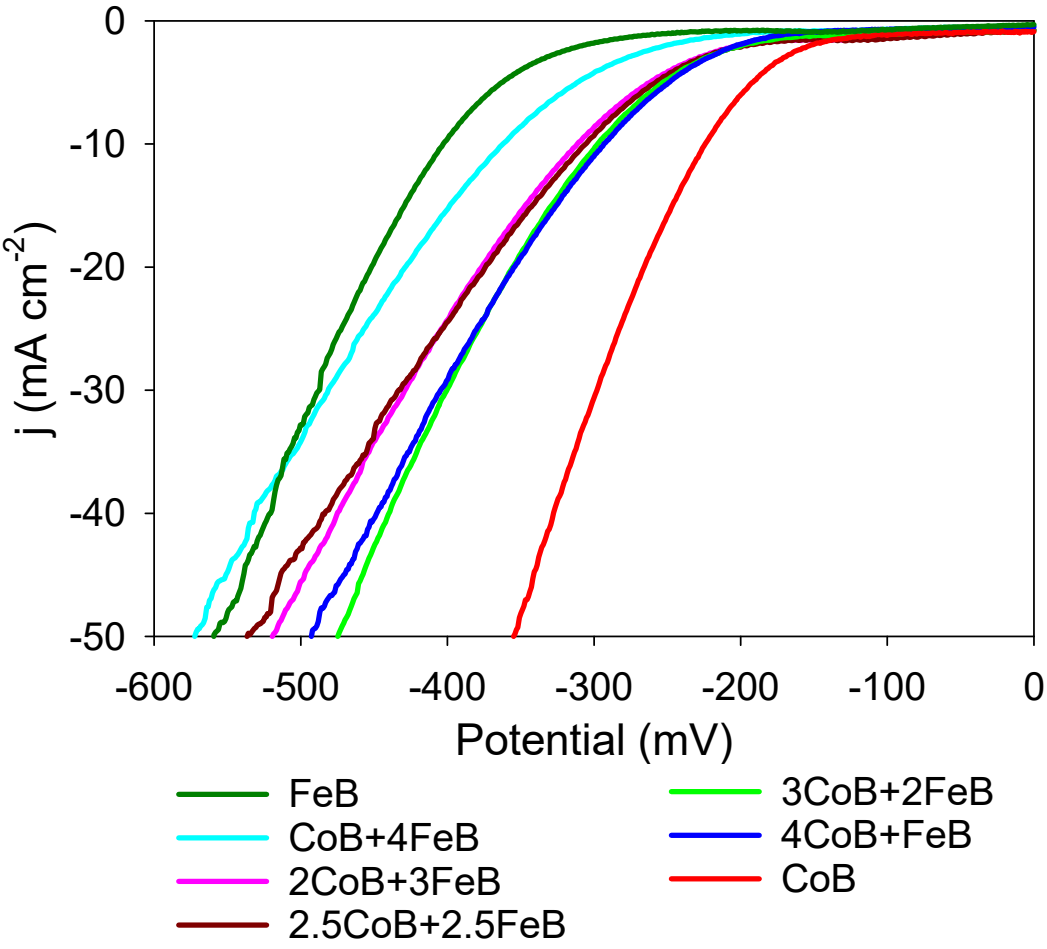

Figure S16. Representative HER LSV results of physically mixed (hand-grinding in a mortar and pestle) CoB + FeB mixtures. Data was obtained using 1.0 M KOH in a three-electrode cell at 5 mV/s scan rate with Hg/HgO reference and graphite rod counter electrodes. Current densities are scaled using the geometric electrode area (0.08 cm^2).

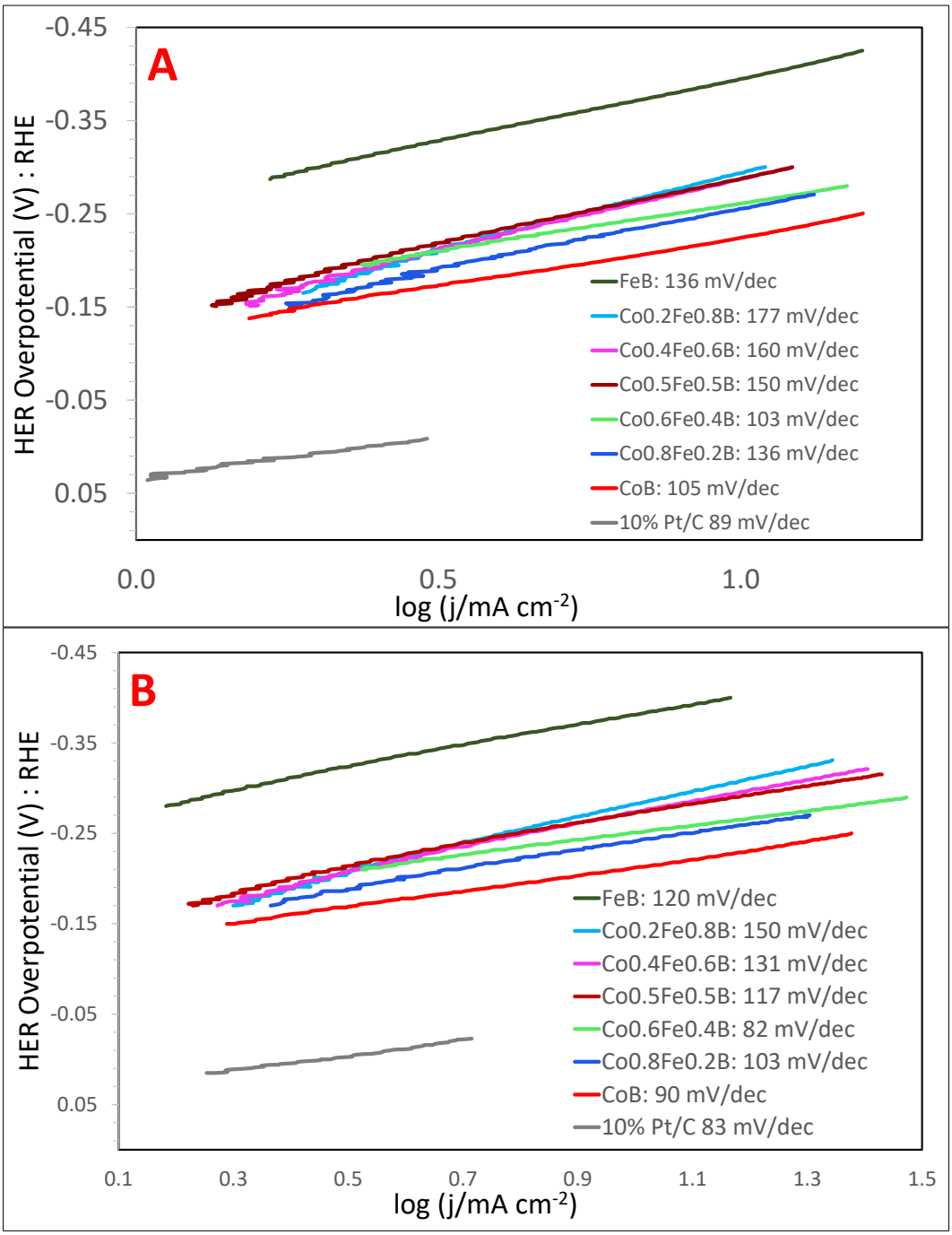

Figure S17. The Tafel slopes of metal borides and 10% Pt/C representative HER LSV runs in 1.0 M KOH. **A**. without iR correction, **B**. with 85% iR correction.

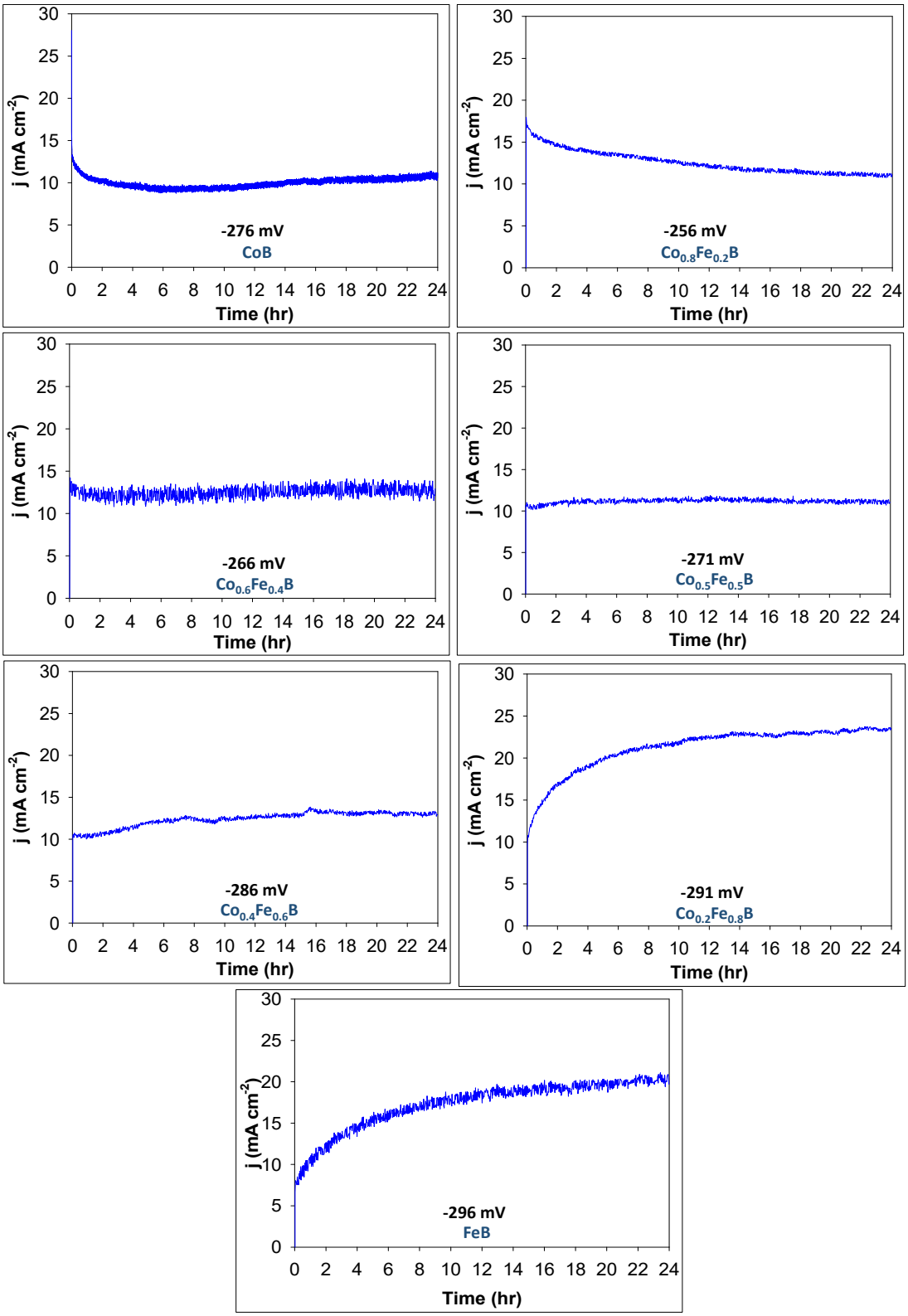

Figure S18. Applied negative potential HER chronoamperometry data (current versus time at constant potential) for metal borides in 1.0 M KOH for 24 hrs. The potentials used are indicated and were chosen to ideally sustain 10 mA cm^{-2}. The working electrodes are metal boride powders embedded on C_{wax} tips.

Table S10. Summary of post-chronoamperometry HER electrocatalysis of SSM synthesized metal borides in 1.0 M KOH (average of 10 HERs were reported in the table) (manually corrected 85% iR compensation results in parentheses).

Sample	(η_{10}) (mV)[1]	(η_{20}) (mV)	Tafel (mV dec^{-1})
CoB	-255 ± 2 (-240 ± 2)	-303 ± 2 (-273 ± 2)	-121 (-103)
$Co_{0.8}Fe_{0.2}B$	-230 ± 6 (-217 ± 6)	-279 ± 4 (-252 ± 4)	-134 (-110)
$Co_{0.6}Fe_{0.4}B$	-264 ± 5 (-254 ± 5)	-303 ± 4 (-282 ± 4)	-119 (-100)
$Co_{0.5}Fe_{0.5}B$	-287 ± 10 (-266 ± 10)	-343 ± 10 (-299 ± 10)	-162 (-138)
$Co_{0.4}Fe_{0.6}B$	-267 ± 8 (-237 ± 8)	-326 ± 8 (-266 ± 8)	-161 (-130)
$Co_{0.2}Fe_{0.8}B$	-275 ± 3 (-257 ± 3)	-335 ± 3 (-298 ± 3)	-170 (-146)
FeB	-324 ± 10 (-306 ± 10)	-382 ± 9 (-346 ± 9)	-169 (-149)

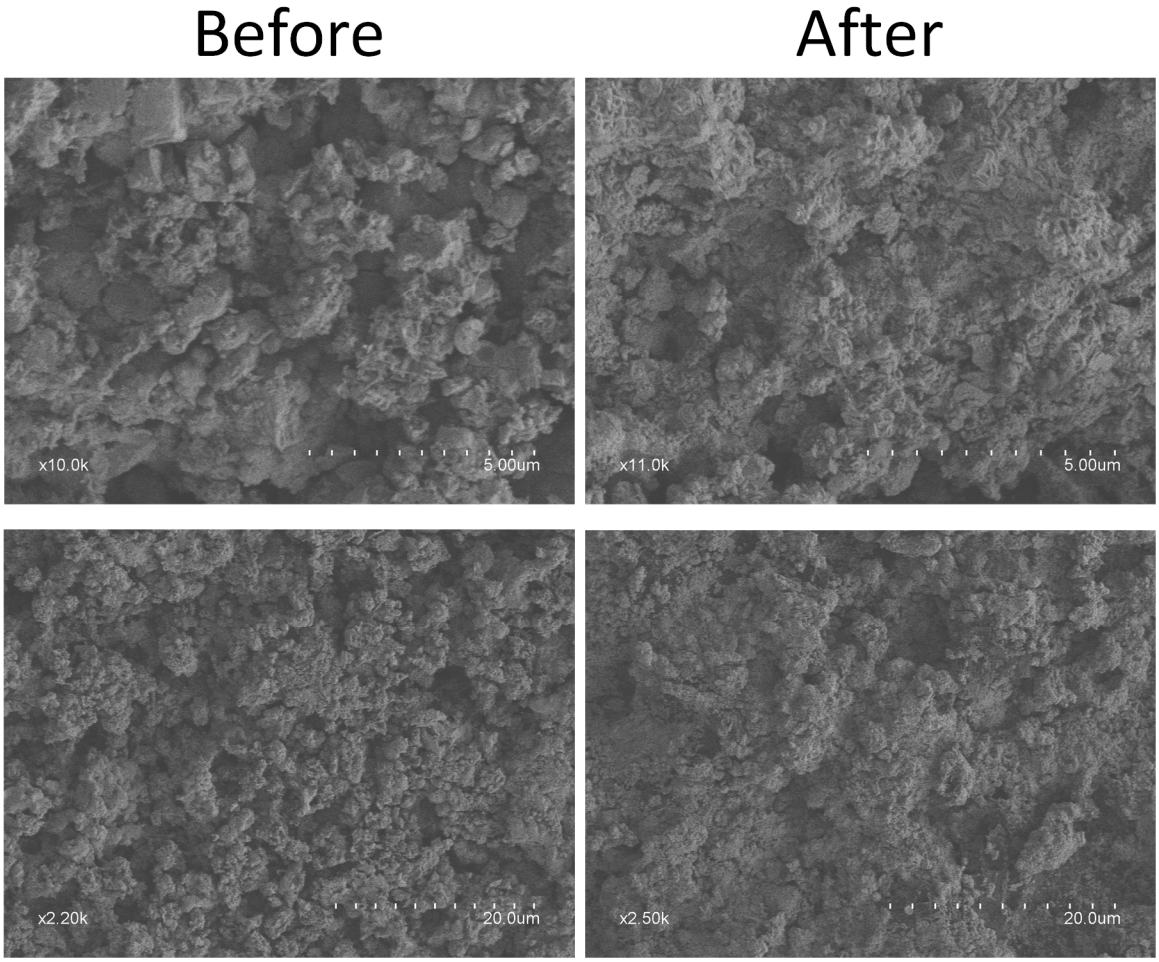

Figure S19. SEM surface comparison of FeB electrodes before (left) and after (right) HER electrochemistry measurements. Top two images are high-magnification (5 μm) and bottom two images are low-magnification (20 μm) images.

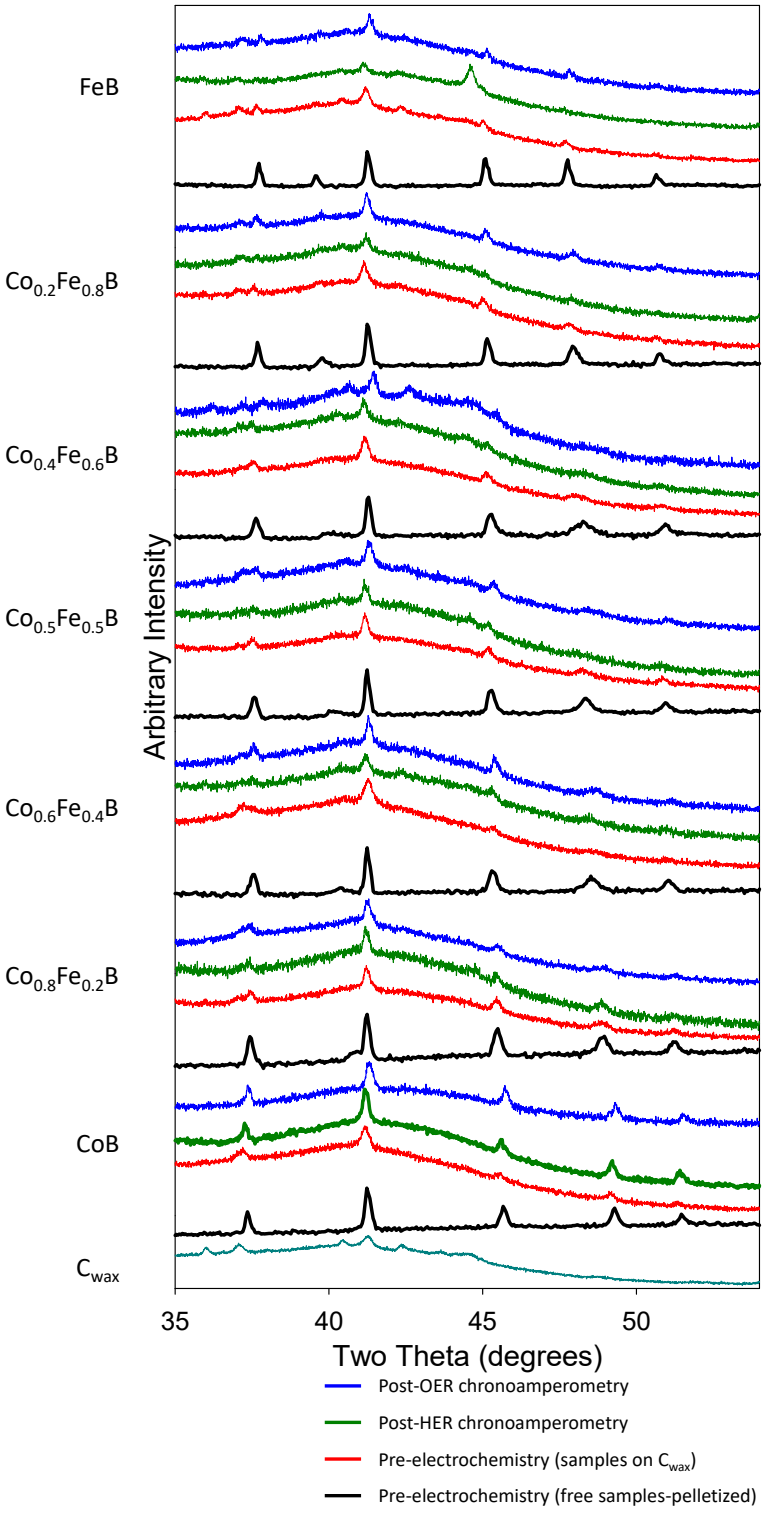

Figure S20. Powder XRD results of pre- and post-positive potential OER chronoamperometry (red and blue diffractograms) and post-negative potential HER chronoamperometry (green diffractograms) of powders on C_{wax} tips for CoB, FeB, and $Co_{1-x}Fe_xB$ solid-solutions. Metal borides pelletized free sample XRDs (black diffractograms), and diffractogram of C_{wax} are also shown for the comparison. The C_{wax} electrode has several broad XRD peaks that are a combination of graphite and paraffin wax diffraction.

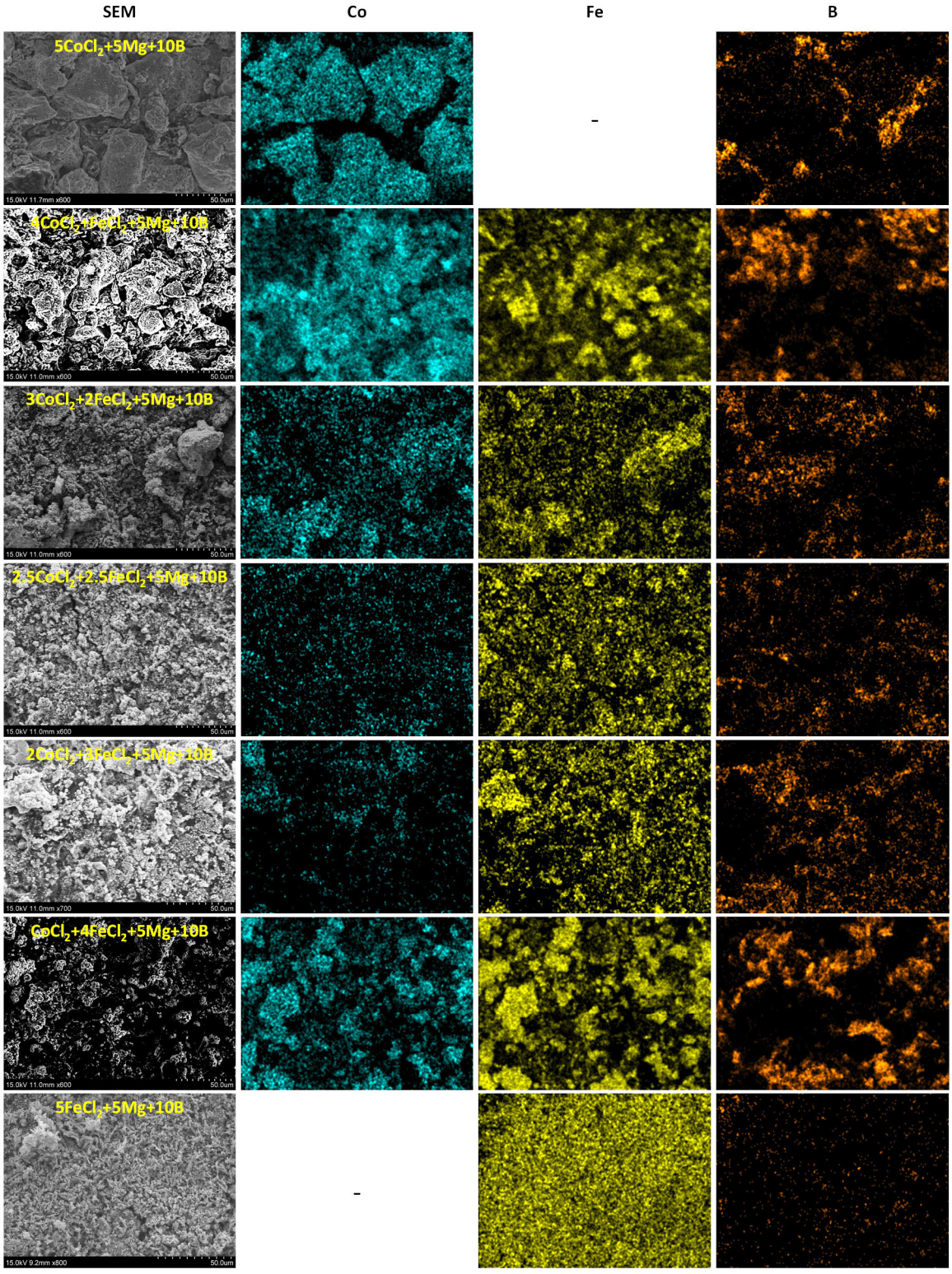

Figure S21. Post-negative potential HER chronoamperometry EDS maps of CoB, FeB, and $Co_{1-x}Fe_xB$ solid-solutions. Images are from powders embedded on C_{wax} tip.

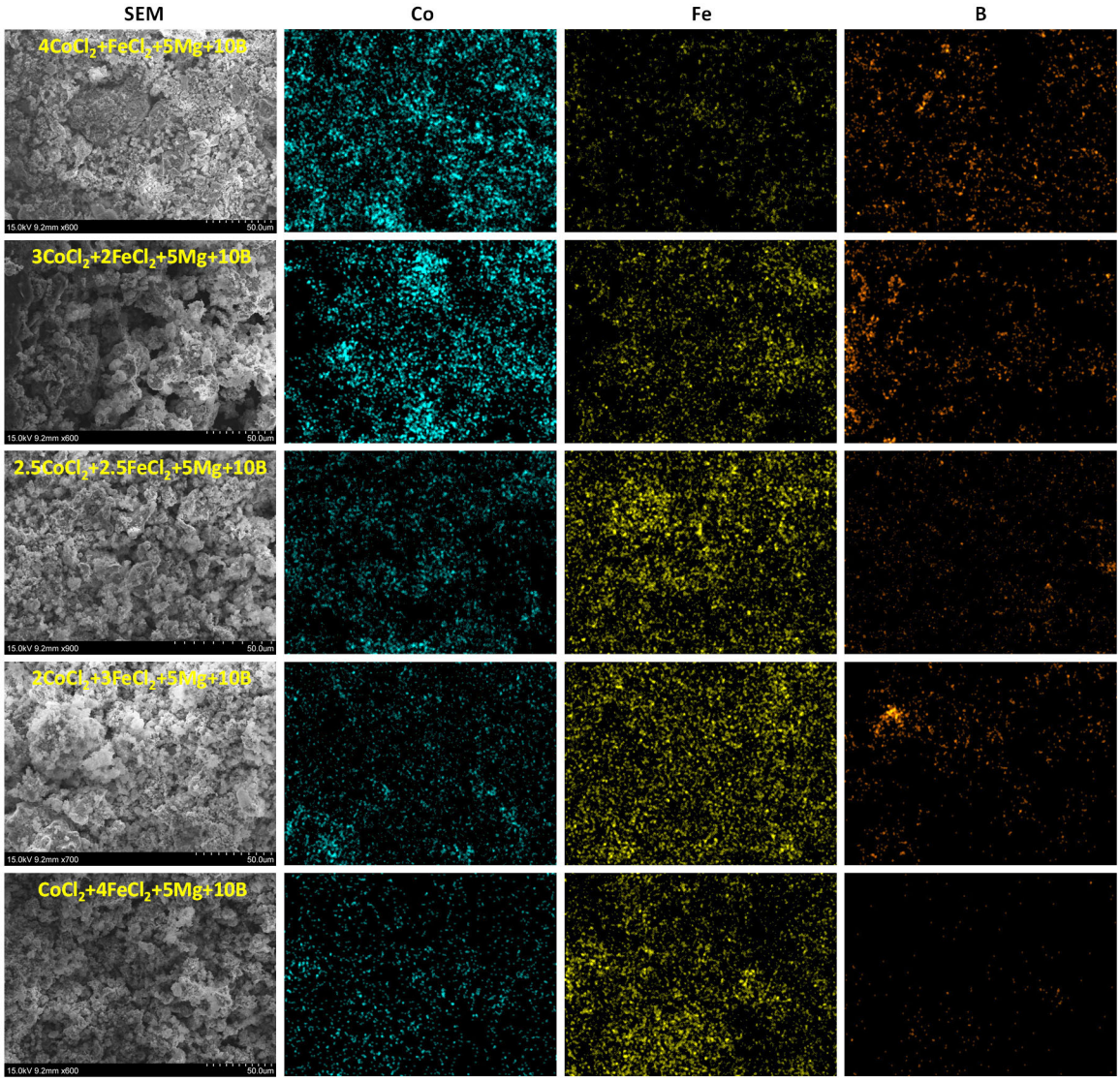

Figure S22. EDS maps of CoB, FeB, and $Co_{1-x}Fe_xB$ solid-solutions on C_{wax} tips before electrochemistry measurements (pre-electrochemistry). Images are from powders embedded on C_{wax} tip.

Table S11. EDS Co/Fe ratios of $Co_{1-x}Fe_xB$ solid-solutions before and after electrochemistry measurements.

Sample	Before electrochemistry (free powder pelletized)	Before electrochemistry (on C_{wax})	After electrochemistry (HER)	After electrochemistry (OER)
	Co/Fe ratio	**Co/Fe ratio**	**Co/Fe ratio**	**Co/Fe ratio**
$4CoCl_2$+$FeCl_2$	78/22	78/22	62/38	78/22
$3CoCl_2$+$2FeCl_2$	55/45	57/43	57/43	63/37
$2.5CoCl_2$+$2.5FeCl_2$	45/55	50/50	32/68	51/49
$2CoCl_2$+$3FeCl_2$	33/67	34/66	23/77	36/64
$CoCl_2$+$4FeCl_2$	19/81	19/81	16/84	23/77

EDS of fresh metal borides as pelletized free powder form or pressed and embedded on C_{wax} electrode tips were used as before electrochemistry EDS samples. EDS of metal borides on C_{wax} after electrochemistry was obtained after initial 50 HERs or 56 OERs, 24-hour chronoamperometry run, and post 10 LSV runs.

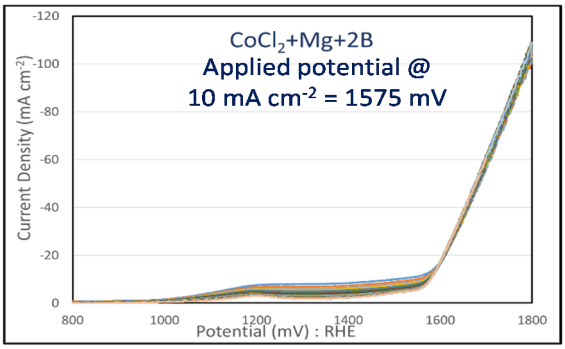
$CoCl_2$+Mg+2B
Applied potential @
10 mA cm^{-2} = 1575 mV
Current Density (mA cm^{-2})
Potential (mV) : RHE

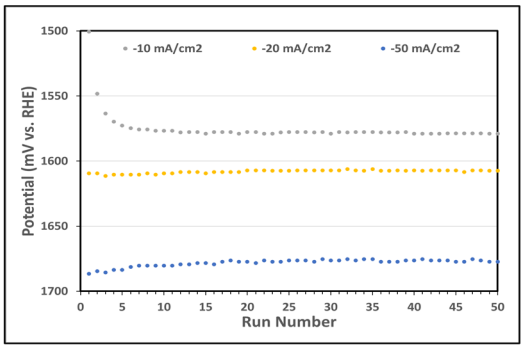
-10 mA/cm2
-20 mA/cm2
-50 mA/cm2
Potential (mV vs. RHE)
Run Number

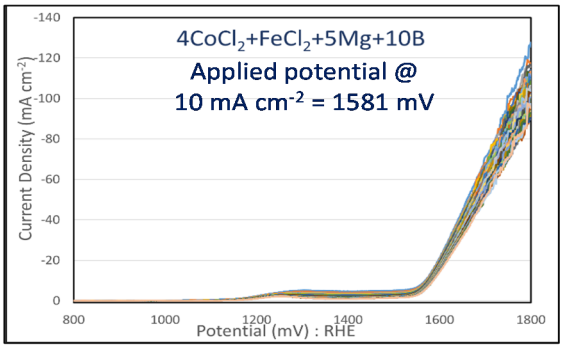
$4CoCl_2$+$FeCl_2$+5Mg+10B
Applied potential @
10 mA cm^{-2} = 1581 mV
Current Density (mA cm^{-2})
Potential (mV) : RHE

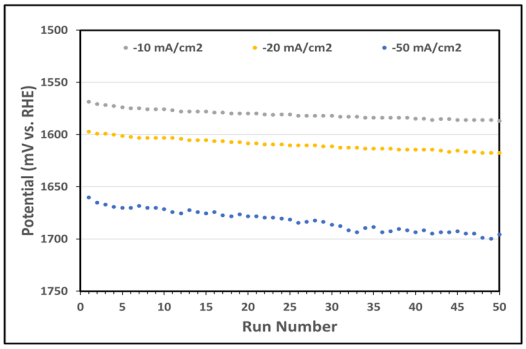
-10 mA/cm2
-20 mA/cm2
-50 mA/cm2
Potential (mV vs. RHE)
Run Number

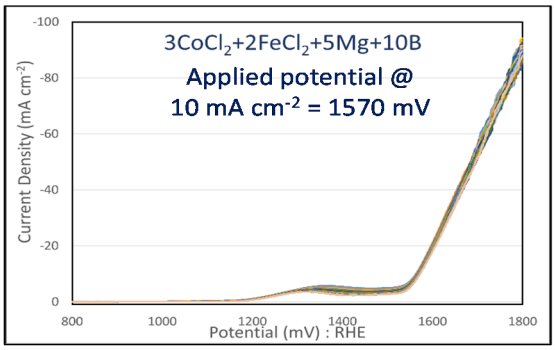
$3CoCl_2$+$2FeCl_2$+5Mg+10B
Applied potential @
10 mA cm^{-2} = 1570 mV
Current Density (mA cm^{-2})
Potential (mV) : RHE

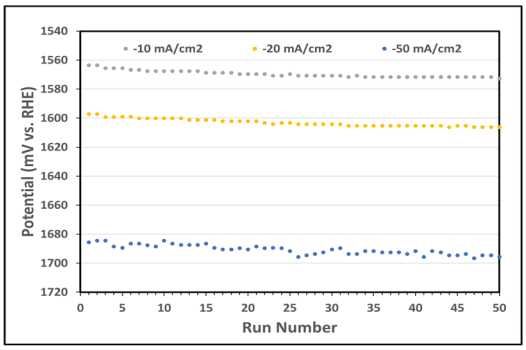
-10 mA/cm2
-20 mA/cm2
-50 mA/cm2
Potential (mV vs. RHE)
Run Number

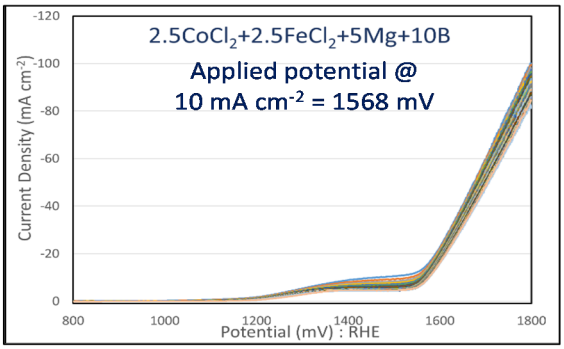
$2.5CoCl_2$+$2.5FeCl_2$+5Mg+10B
Applied potential @
10 mA cm^{-2} = 1568 mV
Current Density (mA cm^{-2})
Potential (mV) : RHE

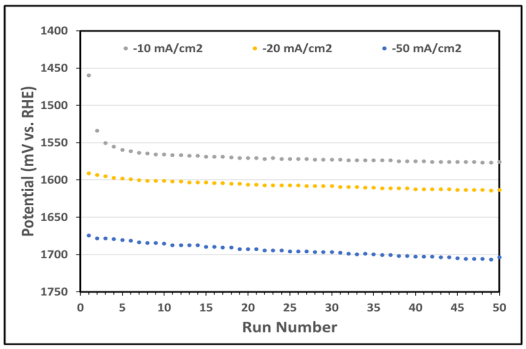
-10 mA/cm2
-20 mA/cm2
-50 mA/cm2
Potential (mV vs. RHE)
Run Number

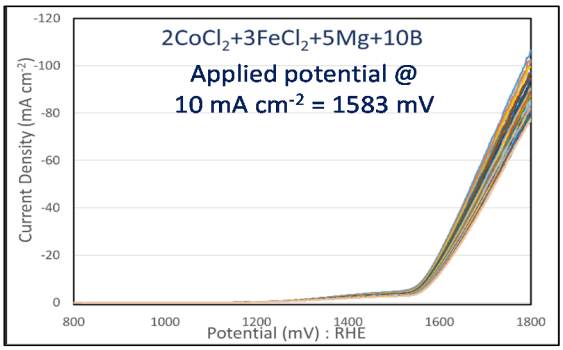
$2CoCl_2$+$3FeCl_2$+5Mg+10B
Applied potential @
10 mA cm^{-2} = 1583 mV
Current Density (mA cm^{-2})
Potential (mV) : RHE

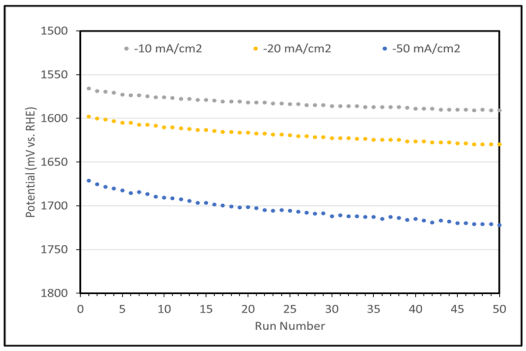
-10 mA/cm2
-20 mA/cm2
-50 mA/cm2
Potential (mV vs. RHE)
Run Number

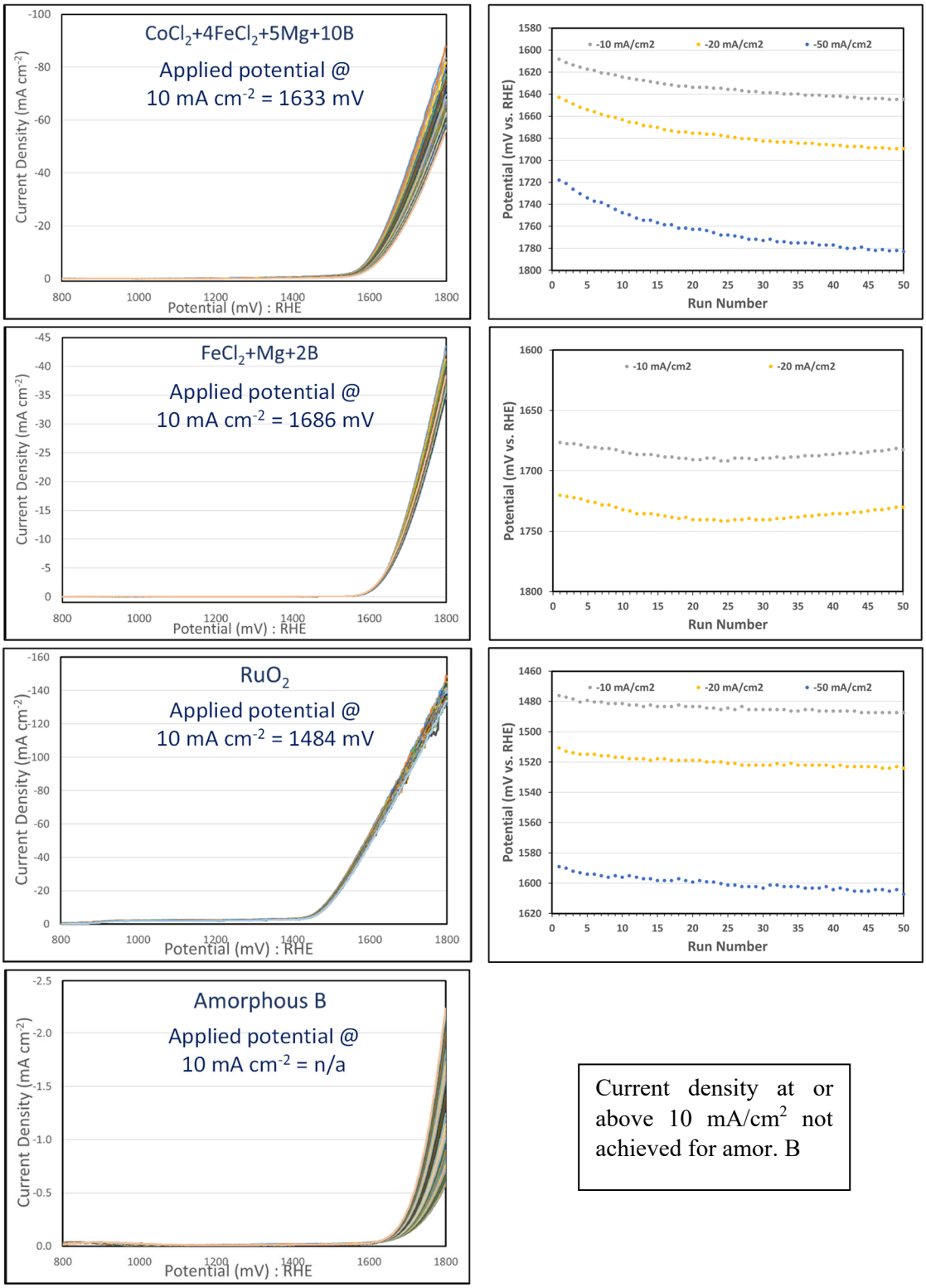

Current density at or above 10 mA/cm^2 not achieved for amor. B

Figure S23. Left column: Overlay plots of 50 LSV runs of CoB, FeB, $Co_{1-x}Fe_xB$, RuO_2, and B for OER experiments in 1.0 M KOH at 5 mV s^{-1} scan rate. Right column: Plots of run number versus potentials at 10, 20 and 50 mA/cm^2 current densities extracted from left column overlay plots. The working electrodes are metal boride powders embedded on C_{wax} tips.

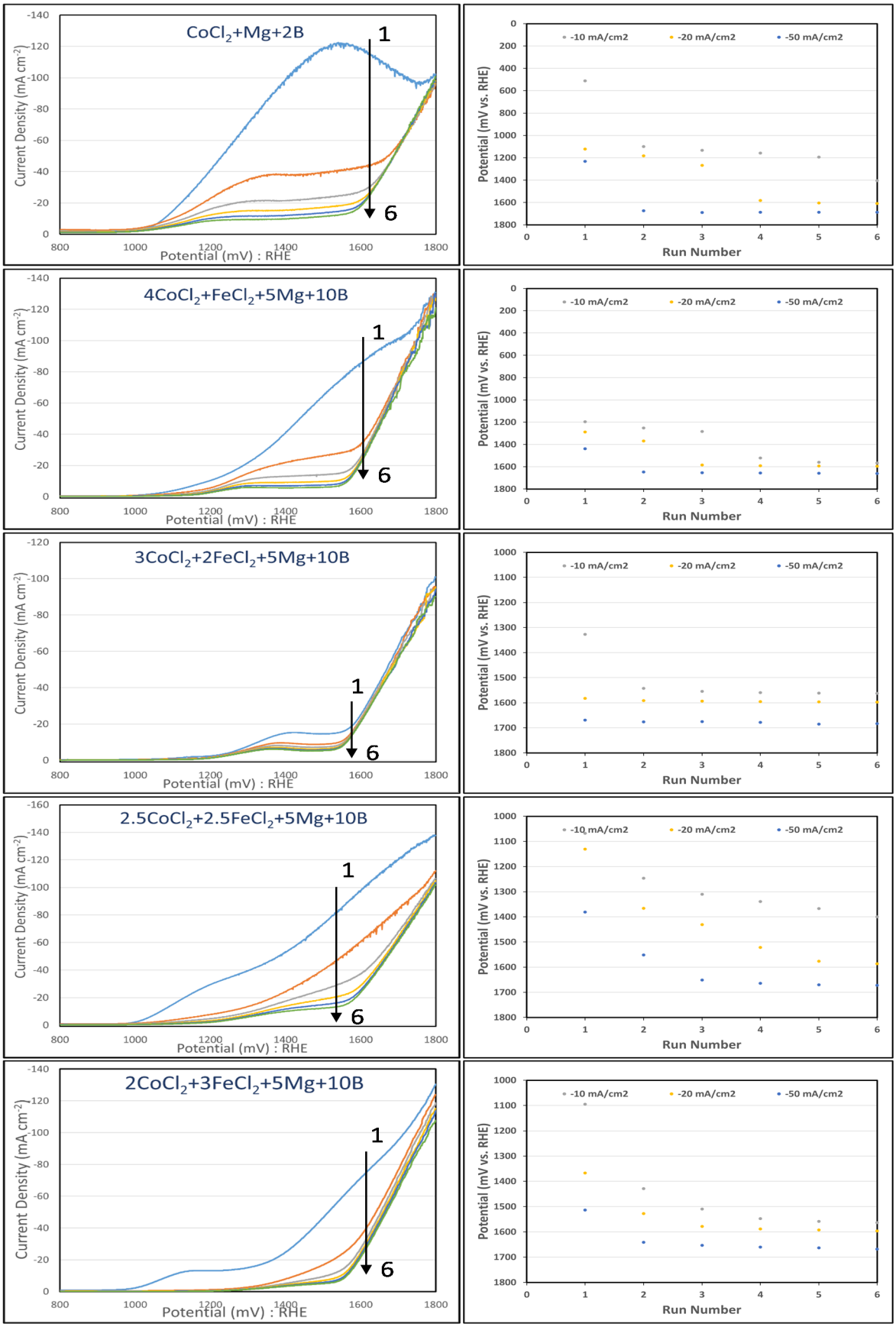
CoCl2+Mg+2B
4CoCl2+FeCl2+5Mg+10B
3CoCl2+2FeCl2+5Mg+10B
2.5CoCl2+2.5FeCl2+5Mg+10B
2CoCl2+3FeCl2+5Mg+10B
Current Density (mA cm-2)
Potential (mV) : RHE
Potential (mV vs. RHE)
Run Number
-10 mA/cm2
-20 mA/cm2
-50 mA/cm2
1
6

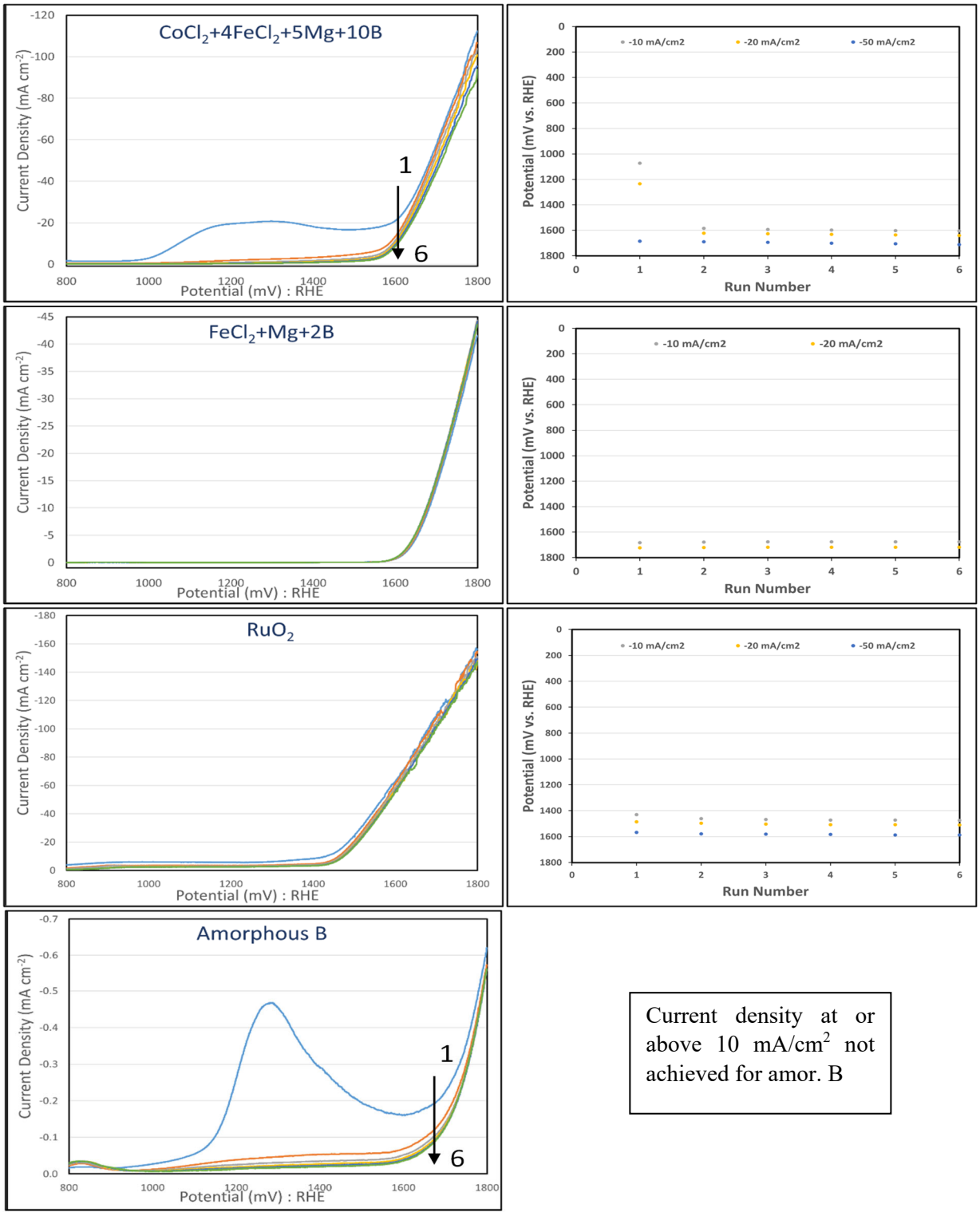

Figure S24. First six OER conditioning runs overlay plots and their corresponding potential versus run number plots in 1.0 M KOH at 5 mV s^{-1} scan rate. The working electrodes are metal boride powders embedded on C_{wax} tips. It is obvious that CoB and $Co_{1-x}Fe_xB$ solid solutions' OER active stable surfaces formed after surface modifications of conditioning runs. LSV curves moved from run 1 to run 6 as represented by the arrow.

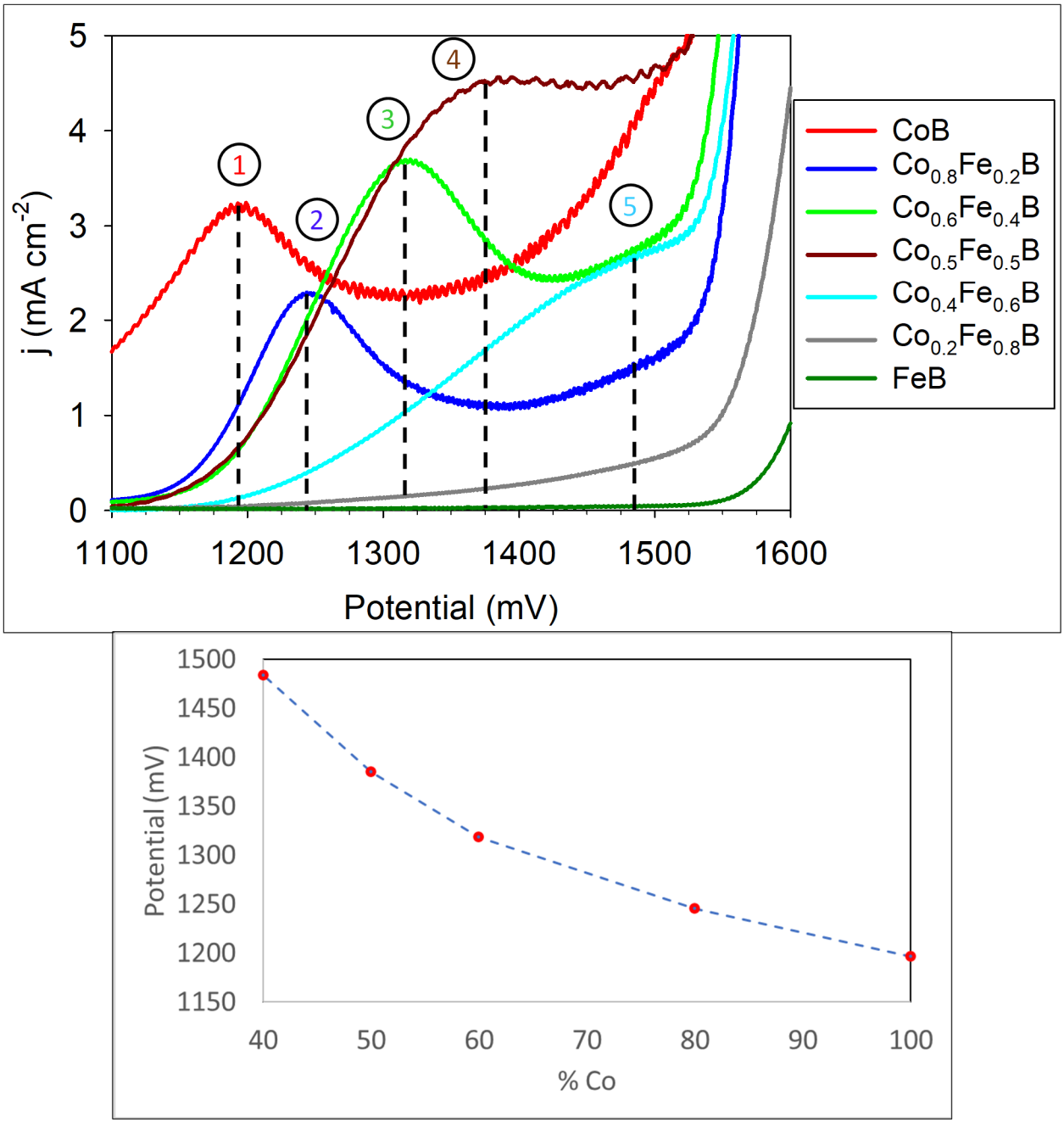

Figure S25. Top: Additional oxidation peak in CoB and $Co_{1-x}Fe_xB$ samples formed around 1200-1500 mV potential range. Representative (25th run) data were obtained for the comparison. Peaks positions at 1196 mV (1), 1245 mV (2), 1318 mV (3), 1385 mV (4), and 1492 mV (5) for CoB, $Co_{0.8}Fe_{0.2}B$, $Co_{0.6}Fe_{0.4}B$, $Co_{0.5}Fe_{0.5}B$, $Co_{0.4}Fe_{0.6}B$ samples, respectively. Bottom: Graph of %Co versus peak potentials.

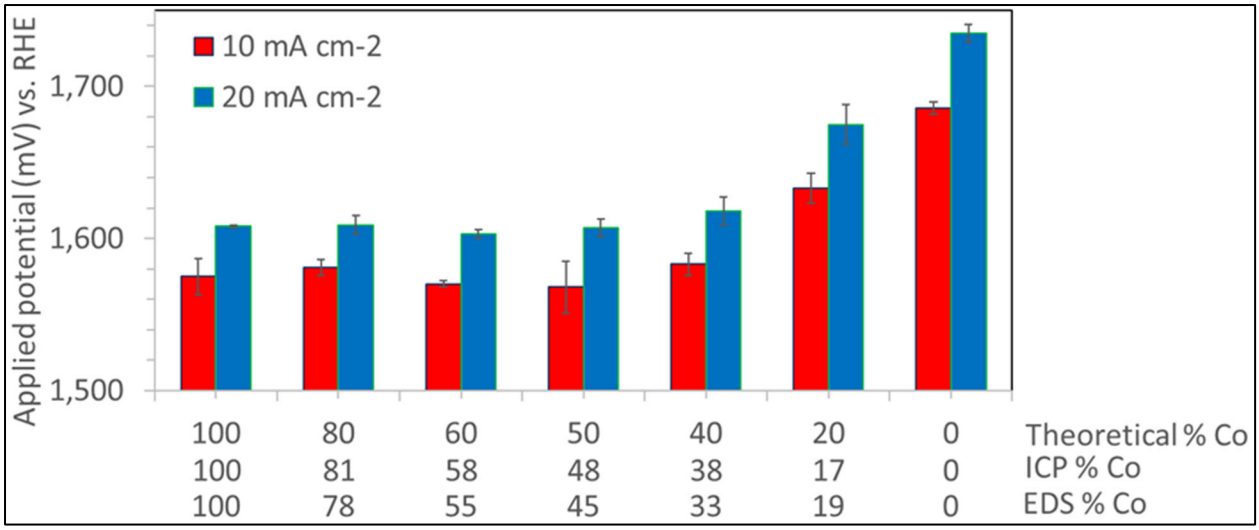

Figure S26. OER current density (10 mA cm^{-2} and 20 mA cm^{-2}) changes with % Co (theoretical, ICP, and EDS).

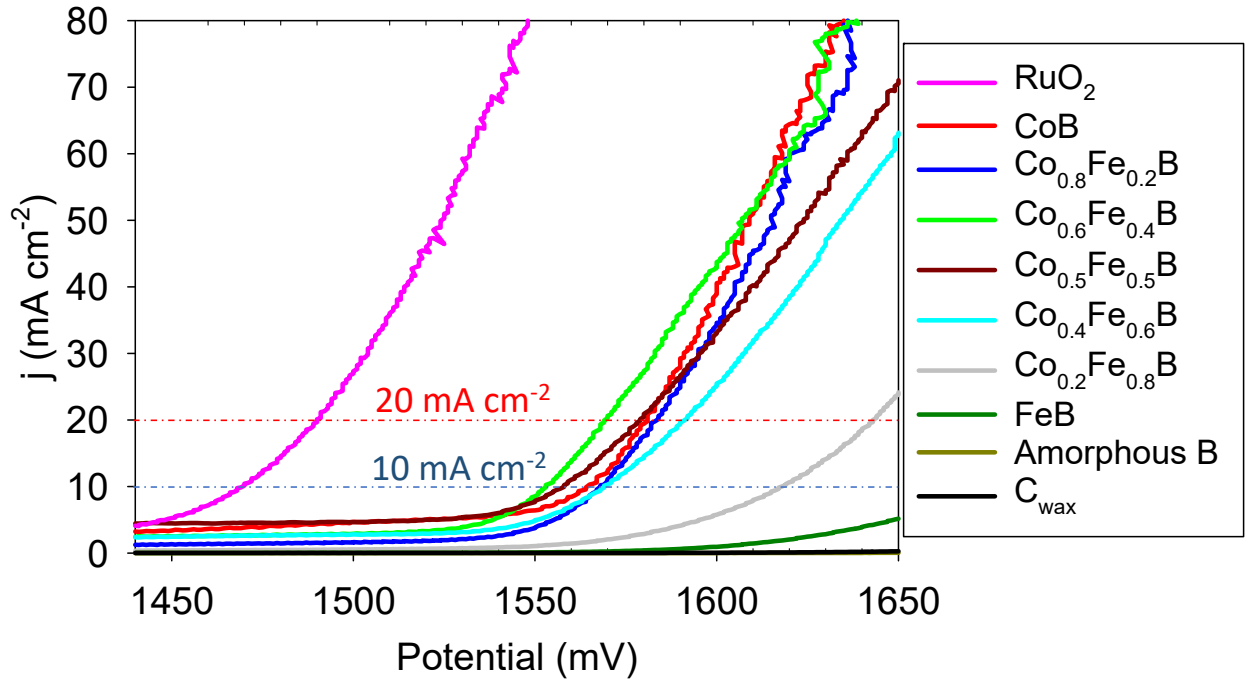

Figure S27. OER LSV overlay plots for metal borides with 85% iR compensation at 5 mV s^{-1} scan rate. A representative LSV run from 10 LSVs with iR on is shown in the graph. The working electrodes are metal boride powders embedded on C_{wax} tips.

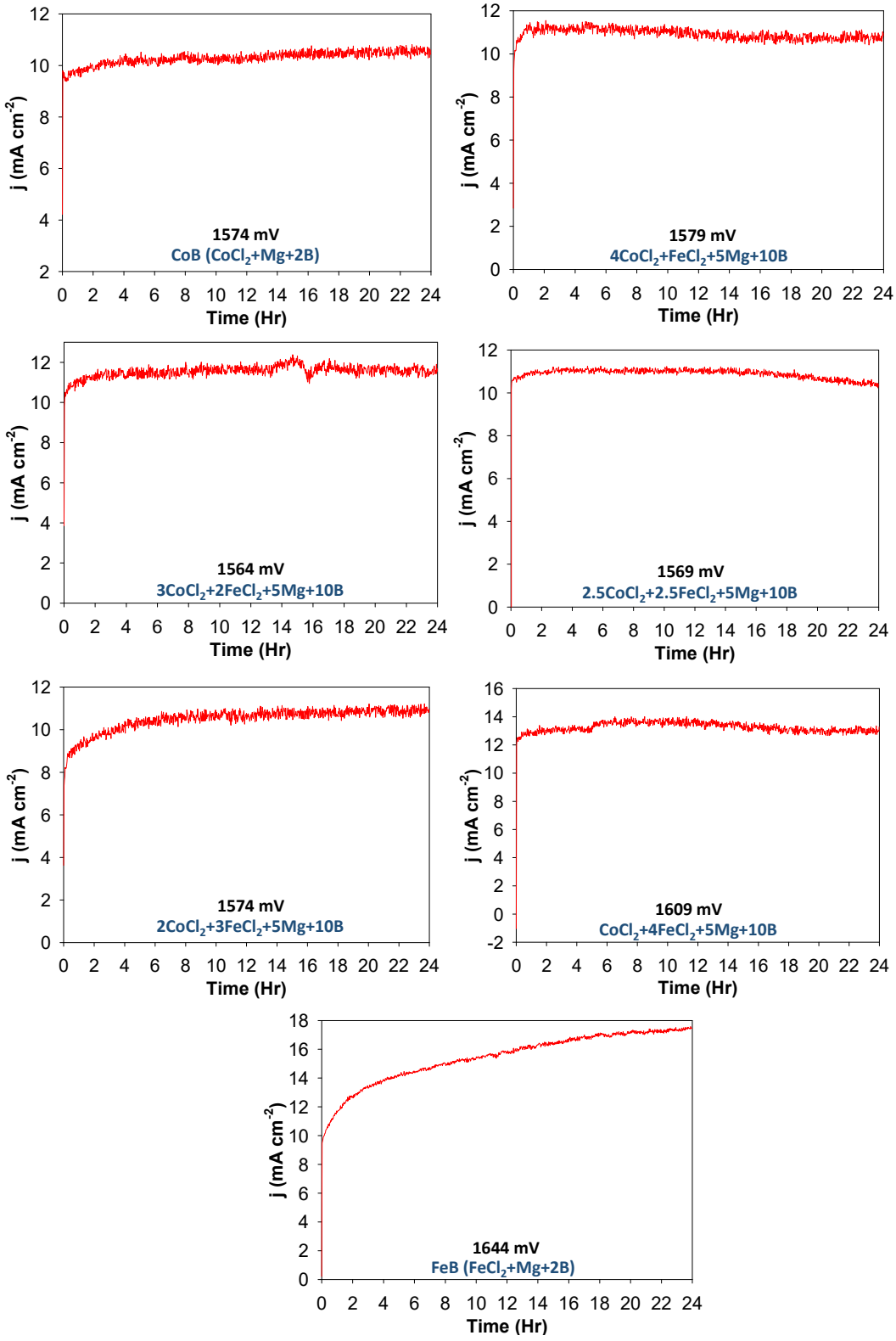

Figure S28. Applied positive potential OER chronoamperometry data (current versus time at constant potential) for metal borides in 1.0 M KOH for 24 hrs. The potentials used are indicated and were chosen to ideally sustain 10 mA/cm^2. The working electrodes are metal boride powders embedded on C_{wax} tips.

Table S12. Summary of post-chronoamperometry OER electrocatalysis of SSM synthesized metal borides in 1.0 M KOH (average of 10 HERs were reported in the table).

Sample	(η_{10}) (mV)[1]	(η_{20}) (mV)	Tafel (mV/dec)
CoB	1572.3±2.9 (1547.9±2.9)	1603.1±2.2 (1554.5±2.4)	102 (48)
$Co_{0.8}Fe_{0.2}B$	1588.4±2.3 (1570.2±2.4)	1621.3±3.3 (1584.9±3.1)	79 (50)
$Co_{0.6}Fe_{0.4}B$	1571.0±1.4 (1562.3±1.3)	1603.1±1.7 (1584.9±1.7)	81 (63)
$Co_{0.5}Fe_{0.5}B$	1577.5±2.0 (1557.4±1.8)	1614.5±2.5 (1574.0±2.7)	109 (55)
$Co_{0.4}Fe_{0.6}B$	1590.2±3.6 (1575.7±3.7)	1626.1±4.7 (1597.0±4.9)	99 (67)
$Co_{0.2}Fe_{0.8}B$	1622.4±6.0 (1607.9±5.9)	1656.7±8.3 (1627.7±8.2)	72 (60)
FeB	1654.7±4.6 (1633.7±4.5)	1690.4±6.0 (1648.8±5.9)	53 (45)

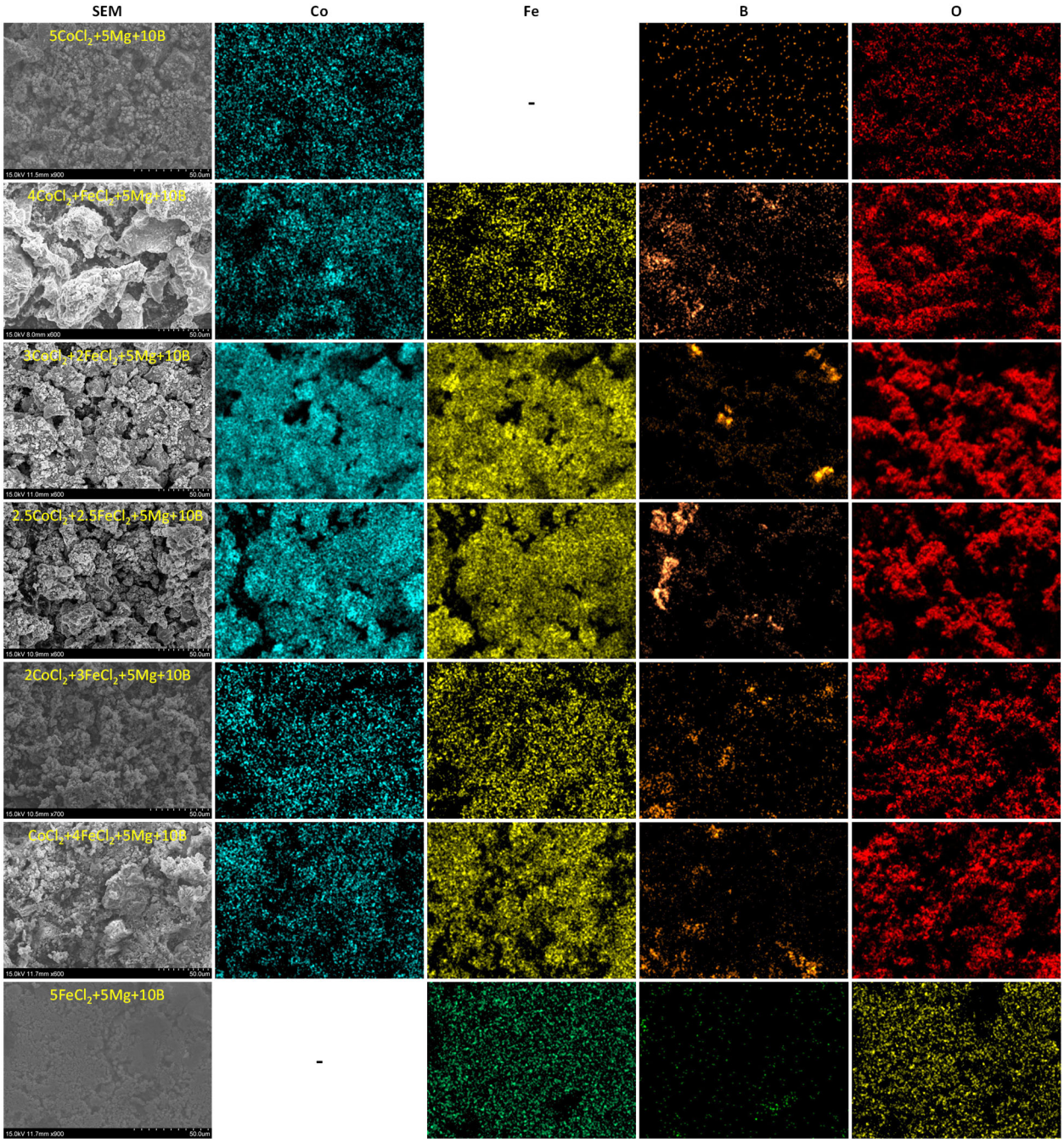

Figure S29. Post-positive potential OER chronoamperometry EDS maps of CoB, FeB, and $Co_{1-x}Fe_xB$ solid-solutions. Images are from powders embedded on C_{wax} tip.

Reference

(1) Rao, L.; Gillan, E. G.; Kaner, R. B. Rapid synthesis of transition-metal borides by solid-state metathesis. *J. Mater. Res.* **1995**, *10* (2), 353-361.
(2) Lupinetti, A. J.; Fife, J. L.; Garcia, E.; Dorhout, P. K.; Abney, K. D. Low-Temperature Synthesis of Uranium Tetraboride by Solid-State Metathesis Reactions. *Inorg. Chem.* **2002**, *41* (9), 2316-2318. DOI: 10.1021/ic015607a.
(3) Aprea, A.; Maspero, A.; Figini Albisetti, A.; Giunchi, G. Synthesis of Alkaline-earth hexaborides, MB_6 (M = Ca, Ba, Sr), by a solid state metathesis (SSM) reaction. *Solid State Sci.* **2012**, *14* (11-12), 1587-1590. DOI: 10.1016/j.solidstatesciences.2012.03.002.
(4) Aprea, A.; Maspero, A.; Masciocchi, N.; Guagliardi, A.; Albisetti, A. F.; Giunchi, G. Nanosized rare-earth hexaborides: Low-temperature preparation and microstructural analysis. *Solid State Sci.* **2013**, *21*, 32-36. DOI: 10.1016/j.solidstatesciences.2013.04.001.
(5) Jothi, P. R.; Zhang, Y.; Scheifers, J. P.; Park, H.; Fokwa, B. P. T. Molybdenum diboride nanoparticles as a highly efficient electrocatalyst for the hydrogen evolution reaction. *Sustainable Energy Fuels* **2017**, *1*, 1928-1934. DOI: 10.1039/c7se00397h.
(6) Li, Q.; Zou, X.; Ai, X.; Chen, H.; Sun, L.; Zou, X. Revealing Activity Trends of Metal Diborides Toward pH-Universal Hydrogen Evolution Electrocatalysts with Pt-Like Activity. *Adv. Energy Mater.* **2019**, *9*, 1803369. DOI: 10.1002/aenm.201803369.
(7) Ai, X.; Zou, X.; Chen, H.; Su, Y.; Feng, X.; Li, Q.; Liu, Y.; Zhang, Y.; Zou, X. Transition-Metal-Boron Intermetallics with Strong Interatomic d-sp Orbital Hybridization for High-Performance Electrocatalysis. *Angew. Chem. Int. Ed.* **2020**, *59* (10), 3961-3965. DOI: 10.1002/anie.201915663.
(8) Zou, X.; Wang, L.; Ai, X.; Chen, H.; Zou, X. Crystal phase-dependent electrocatalytic hydrogen evolution performance of ruthenium-boron intermetallics. *Chem. Commun.* **2020**, *56* (20), 3061-3064. DOI: 10.1039/d0cc00070a.
(9) Abeysinghe, J. P.; Kolln, A. F.; Gillan, E. G. Rapid and Energetic Solid-State Metathesis Reactions for Iron, Cobalt, and Nickel Boride Formation and Their Investigation as Bifunctional Water Splitting Electrocatalysts. *ACS Mater. Au* **2022**, *2* (4), 489-504. DOI: 10.1021/acsmaterialsau.1c00079.
(10) Binnewies, M.; Milke, E. *Thermochemical Data of Elements and Compounds*; Weinheim, 1999.
(11) Kubaschewski, O.; Alcock, C. B. *Metallurgical Thermochemistry*; Pergamon Press Inc., Maxwell House, 1979. *CRC Handbook of Chemistry and Physics, 102nd Edition (Internet Version 2021)*; Rumble, J. R., Ed.; CRC Press/Taylor & Francis. NIST Chemistry Webbook. Standard Reference Database. (accessed 7/5/2021).
(12) Li, H.; Wen, P.; Li, Q.; Dun, C.; Xing, J.; Lu, C.; Adhikari, S.; Jiang, L.; Carroll, D. L.; Geyer, S. M. Earth-Abundant Iron Diboride (FeB_2) Nanoparticles as Highly Active Bifunctional Electrocatalysts for Overall Water Splitting. *Adv. Energy Mater.* **2017**, *7* (17), 1700513. DOI: 10.1002/aenm.201700513.
(13) Ma, X.; Wen, J.; Zhang, S.; Yuan, H.; Li, K.; Yan, F.; Zhang, X.; Chen, Y. Crystal Co_xB (x = 1-3) Synthesized by a Ball-Milling Method as High-Performance Electrocatalysts for the Oxygen Evolution Reaction. *ACS Sustainable Chem. Eng.* **2017**, *5* (11), 10266-10274. DOI: 10.1021/acssuschemeng.7b02281.
(14) Klemenz, S.; Schuch, J.; Hawel, S.; Zieschang, A.-M.; Kaiser, B.; Jaegermann, W.; Albert, B. Synthesis of a Highly Efficient Oxygen-Evolution Electrocatalyst by Incorporation of Iron into Nanoscale Cobalt Borides. *ChemSusChem* **2018**, *11* (18), 3150-3156. DOI: 10.1002/cssc.201801547.
(15) Masa, J.; Weide, P.; Peeters, D.; Sinev, I.; Xia, W.; Sun, Z.; Somsen, C.; Muhler, M.; Schuhmann, W. Amorphous Cobalt Boride (Co_2B) as a Highly Efficient Nonprecious Catalyst for Electrochemical Water Splitting: Oxygen and Hydrogen Evolution. *Adv. Energy Mater.* **2016**, *6*, 1502313. DOI: 10.1002/aenm.201502313.

(16) Xu, X.; Deng, Y.; Gu, M.; Sun, B.; Liang, Z.; Xue, Y.; Guo, Y.; Tian, J.; Cui, H. Large-scale synthesis of porous nickel boride for robust hydrogen evolution reaction electrocatalyst. *Appl. Surf. Sci.* **2019**, *470*, 591-595. DOI: 10.1016/j.apsusc.2018.11.127.
(17) Masa, J.; Piontek, S.; Wilde, P.; Antoni, H.; Eckhard, T.; Chen, Y.-T.; Muhler, M.; Apfel, U.-P.; Schuhmann, W. Ni-Metalloid (B, Si, P, As, and Te) Alloys as Water Oxidation Electrocatalysts. *Adv. Energy Mater.* **2019**, *9*, 1900796. DOI: 10.1002/aenm.201900796.
(18) Jothi, P. R.; Zhang, Y.; Yubuta, K.; Culver, D. B.; Conley, M.; Fokwa, B. P. T. Abundant Vanadium Diboride with Graphene-like Boron layers for Hydrogen Evolution. *ACS Appl. Energy Mater.* **2019**, *2* (1), 176-181. DOI: 10.1021/acsaem.8b01615.
(19) Mazanek, V.; Nahdi, H.; Luxa, J.; Sofer, Z.; Pumera, M. Electrochemistry of layered metal diborides. *Nanoscale* **2018**, *10* (24), 11544-11552. DOI: 10.1039/c8nr02142b.
(20) Kirshenbaum, M. J.; Richter, M. H.; Dasog, M. Electrochemical Water Oxidation in Acidic Solution Using Titanium Diboride (TiB_2) Catalyst. *ChemCatChem* **2019**, *11* (16), 3877-3881. DOI: 10.1002/cctc.201801736.
(21) Lim, C. S.; Sofer, Z.; Mazanek, V.; Pumera, M. Layered titanium diboride: towards exfoliation and electrochemical applications. *Nanoscale* **2015**, *7* (29), 12527-12534. DOI: 10.1039/c5nr02692j.
(22) Zhuang, Z.; Li, Y.; Li, Z.; Lv, F.; Lang, Z.; Zhao, K.; Zhou, L.; Moskaleva, L.; Guo, S.; Mai, L. MoB/g-C_3N_4 Interface Materials as a Schottky Catalyst to Boost Hydrogen Evolution. *Angew. Chem. Int. Ed.* **2018**, *57* (2), 496-500. DOI: 10.1002/anie.201708748.
(23) Wang, Y.; Mayorga-Martinez, C. C.; Chia, X. Y.; Sofer, Z.; Latiff, N. M.; Pumera, M. Bipolar Electrochemistry as a Simple Synthetic Route toward Nanoscale Transition of Mo_2B_5 and W_2B_5 for Enhanced Hydrogen Evolution Reaction. *ACS Sustainable Chem. Eng.* **2019**, *7* (14), 12148-12159. DOI: 10.1021/acssuschemeng.9b01251.
(24) Guo, F.; Wu, Y.; Ai, X.; Chen, H.; Li, G.-D.; Chen, W.; Zou, X. A class of metal diboride electrocatalysts synthesized by a molten salt-assisted reaction for the hydrogen evolution reaction. *Chem. Commun.* **2019**, *55* (59), 8627-8630. DOI: 10.1039/c9cc03638e.
(25) Nsanzimana, J. M. V.; Peng, Y.; Xu, Y. Y.; Thia, L.; Wang, C.; Xia, B. Y.; Wang, X. An Efficient and Earth-Abundant Oxygen-Evolving Electrocatalyst Based on Amorphous Metal Borides. *Adv. Energy Mater.* **2018**, *8*, 1701475. DOI: 10.1002/aenm.201701475.
(26) Zieschang, A.-M.; Bocarsly, J. D.; Schuch, J.; Reichel, C. V.; Kaiser, B.; Jaegermann, W.; Seshadri, R.; Albert, B. Magnetic and Electrocatalytic Properties of Nanoscale Cobalt Boride, Co_3B. *Inorg. Chem.* **2019**, *58*, 16609-16617. DOI: 10.1021/acs.inorgchem.9b02617.
(27) Gupta, S.; Patel, N.; Miotello, A.; Kothari, D. C. Cobalt-Boride: An efficient and robust electrocatalyst for Hydrogen Evolution Reaction. *J. Power Sources* **2015**, *279*, 620-625. DOI: 10.1016/j.jpowsour.2015.01.009.
(28) Gupta, S.; Patel, N.; Fernandes, R.; Kadrekar, R.; Dashora, A.; Yadav, A. K.; Bhattacharyya, D.; Jha, S. N.; Miotello, A.; Kothari, D. C. Co–Ni–B nanocatalyst for efficient hydrogen evolution reaction in wide pH range. *Appl. Catal. B* **2016**, *192*, 126-133. DOI: 10.1016/j.apcatb.2016.03.032.
(29) Li, Y.; Xu, H.; Huang, H.; Gao, L.; Zhao, Y.; Ma, T. Synthesis of Co–B in porous carbon using a metal-organic framework (MOF) precursor: A highly efficient catalyst for the oxygen evolution reaction. *Electrochem. Commun.* **2018**, *86*, 140-144.
(30) Jiang, Y.; Fang, Y.; Chen, C.; Ni, P.; Kong, B.; Song, Z.; Lu, Y.; Niu, L. Amorphous Cobalt Boride Nanosheets Directly Grown on Nickel Foam: Controllable Alternately Dipping Deposition for Efficient Oxygen Evolution. *ChemElectroChem* **2019**, *6* (14), 3684-3689. DOI: 10.1002/celc.201900897.
(31) Hao, W.; Wu, R.; Zhang, R.; Ha, Y.; Chen, Z.; Wang, L.; Yang, Y.; Ma, X.; Sun, D.; Fang, F.; et al. Electroless Plating of Highly Efficient Bifunctional Boride-Based Electrodes toward Practical Overall Water Splitting. *Adv. Energy Mater.* **2018**, *8* (26), 1801372. DOI: 10.1002/aenm.201801372.

(32) Tan, T.; Han, P.; Cong, H.; Cheng, G.; Luo, W. An Amorphous Cobalt Borate Nanosheet-Coated Cobalt Boride Hybrid for Highly Efficient Alkaline Water Oxidation Reaction. *ACS Sustainable Chem. Eng.* **2019**, *7*, 5620-5625. DOI: 10.1021/acssuschemeng.9b00258.
(33) Arivu, M.; Masud, J.; Umapathi, S.; Nath, M. Facile synthesis of Ni_3B/rGO nanocomposite as an efficient electrocatalyst for the oxygen evolution reaction in alkaline media. *Electrochem. Commun.* **2018**, *86*, 121-125. DOI: 10.1016/j.elecom.2017.12.002.
(34) Masa, J.; Andronescu, C.; Antoni, H.; Sinev, I.; Seisel, S.; Elumeeva, K.; Barwe, S.; Marti-Sanchez, S.; Arbiol, J.; Cuenya, B. R.; et al. Role of Boron and Phosphorus in Enhanced Electrocatalytic Oxygen Evolution by Nickel Borides and Nickel Phosphides. *ChemElectroChem* **2019**, *6*, 235-240. DOI: 10.1002/celc.201800669.
(35) Zeng, M.; Wang, H.; Zhao, C.; Wei, J.; Qi, K.; Wang, W.; Bai, X. Nanostructured Amorphous Nickel Boride for High-Efficiency Electrocatalytic Hydrogen Evolution over a Broad pH Range. *ChemCatChem* **2016**, *8* (4), 708-712. DOI: 10.1002/cctc.201501221.
(36) Cao, M.; Zhang, X.; Qin, J.; Liu, R. Enhancement of Hydrogen Evolution Reaction Performance of Graphitic Carbon Nitride with Incorporated Nickel Boride. *ACS Sustainable Chem. Eng.* **2018**, *6* (12), 16198-16204. DOI: 10.1021/acssuschemeng.8b02994.
(37) Zhao, S.; Xu, S.; Yao, J.; Chen, N.; Gong, Y.; Zhang, X.; Hao, X.; Zhang, L.; Pei, C.; Tian, R.; et al. Elucidating the reaction pathway of crystalline multi-metal borides for highly efficient oxygen-evolving electrocatalysts. *J. Mater. Chem. A* **2022**, *10* (3), 1569-1578. DOI: 10.1039/d1ta09078j.
(38) Zou, X.; Zhang, W.; Zhou, X.; Song, K.; Ge, X.; Zheng, W. The surface of metal boride tinted by oxygen evolution reaction for enhanced water electrolysis. *J. Energy Chem.* **2022**, *72*, 509-515. DOI: 10.1016/j.jechem.2022.05.0392095-4956.
(39) Patil, K.; Babar, P.; Li, X.; Karade, V.; Kim, S.; Jang, S. Y.; Bhoite, P.; Kim, J. H. Co–Fe–B Nanochain Electrocatalysts for Oxygen Evolution at High Current Density. *ACS Appl. Nano Mater.* **2022**, *5* (5), 6260-6267. DOI: 10.1021/acsanm.2c00312.
(40) Liu, X.; He, G.; Liu, H.; Zhu, Y.; Xiao, J.; Han, L. Boron-doped cobalt-iron bimetal phosphides nanosheets for enhanced oxygen evolution. *J. Alloys Compd.* **2022**, *893*. DOI: 10.1016/j.jallcom.2021.162208.
(41) Wang, N.; Xu, A.; Ou, P.; Hung, S. F.; Ozden, A.; Lu, Y. R.; Abed, J.; Wang, Z.; Yan, Y.; Sun, M. J.; et al. Boride-derived oxygen-evolution catalysts. *Nat. Commun.* **2021**, *12* (1), 6089. DOI: 10.1038/s41467-021-26307-7.
(42) Qiang, C.; Zhang, L.; He, H.; Liu, Y.; Zhao, Y.; Sheng, T.; Liu, S.; Wu, X.; Fang, Z. Efficient electrocatalytic water splitting by bimetallic cobalt iron boride nanoparticles with controlled electronic structure. *J. Colloid Interface Sci.* **2021**, *604*, 650-659. DOI: 10.1016/j.jcis.2021.07.024.
(43) Nsanzimana, J. M. V.; Gong, L.; Dangol, R.; Reddu, V.; Jose, V.; Xia, B. Y.; Yan, Q.; Lee, J. M.; Wang, X. Tailoring of Metal Boride Morphology via Anion for Efficient Water Oxidation. *Adv. Energy Mater.* **2019**, *9* (28), 1901503. DOI: 10.1002/aenm.201901503.
(44) Mann, D. K.; Xu, J.; Mordvinova, N. E.; Yannello, V.; Ziouani, Y.; Gonzalez-Ballesteros, N.; Sousa, J. P. S.; Lebedev, O. I.; Kolen'ko, Y. V.; Shatruk, M. Electrocatalytic water oxidation over $AlFe_2B_2$. *Chem. Sci.* **2019**, *10* (9), 2796-2804. DOI: 10.1039/c8sc04106g.
(45) Li, Y.; Huang, B.; Sun, Y.; Luo, M.; Yang, Y.; Qin, Y.; Wang, L.; Li, C.; Lv, F.; Zhang, W.; et al. Multimetal Borides Nanochains as Efficient Electrocatalysts for Overall Water Splitting. *Small* **2019**, *15*, 1804212. DOI: 10.1002/smll.201804212.
(46) Sheng, M.; Wu, Q.; Wang, Y.; Liao, F.; Zhou, Q.; Hou, J.; Weng, W. Network-like porous Co-Ni-B grown on carbon cloth as efficient and stable catalytic electrodes for hydrogen evolution. *Electrochem. Commun.* **2018**, *93*, 104-108. DOI: 10.1016/j.elecom.2018.06.017.

(47) Gupta, S.; Patel, N.; Fernandes, R.; Hanchate, S.; Miotello, A.; Kothari, D. C. Co-Mo-B Nanoparticles as a non-precious and efficient Bifunctional Electrocatalyst for Hydrogen and Oxygen Evolution. *Electrochim. Acta* **2017**, *232*, 64-71. DOI: 10.1016/j.electacta.2017.02.100.
(48) Chen, H.; Ouyang, S.; Zhao, M.; Li, Y.; Ye, J. Synergistic Activity of Co and Fe in Amorphous Co*x*-Fe-B Catalyst for Efficient Oxygen Evolution Reaction. *ACS Appl. Mater. Interfaces* **2017**, *9* (46), 40333-40343. DOI: 10.1021/acsami.7b13939.